FREQUENCY-DOMAIN SIMULATION OF SOUND PROPAGATION IN ACOUSTICALLY TREATED DUCTS WITH FLOW

A THESIS SUBMITTED TO
THE GRADUATE SCHOOL OF NATURAL AND APPLIED SCIENCES
OF
THE MIDDLE EAST TECHNICAL UNIVERSITY

BY

AHMET ŞİRZAİ

IN PARTIAL FULFILLMENT OF THE REQUIREMENTS FOR THE DEGREE OF
MASTER OF SCIENCE
IN
THE DEPARTMENT OF AERONAUTICAL ENGINEERING

AUGUST 2000

Approval of the Graduate School of Natural and Applied Sciences.

Prof. Dr. Tayfur ÖZTÜRK
Director

I certify that this thesis satisfies all the requirements as a thesis for the degree of Master of Science.

Prof. Dr. Nafiz ALEMDAROĞLU
Head of Department

This is to certify that I have read this thesis and that in my opinion it is fully adequate, in scope and quality, as a thesis for the degree of Master of Science.

Assoc. Prof. Dr. Yusuf ÖZYÖRÜK
Supervisor

Examining Committee Members

Prof. Dr. Nafiz ALEMDAROĞLU

Prof. Dr. M.Cevdet ÇELENLİGİL

Assoc. Prof. Dr. M.Zülfü AŞIK

Assoc. Prof. Dr. Yusuf ÖZYÖRÜK

Assoc. Prof. Dr. İsmail H. TUNCER

ABSTRACT

FREQUENCY-DOMAIN SIMULATION OF SOUND PROPAGATION IN ACOUSTICALLY TREATED DUCTS WITH FLOW

Şirzai, Ahmet
M.S., Department of Aeronautical Engineering
Supervisor: Assoc. Prof. Dr. Yusuf Özyörük.

August 2000, 71 pages

A frequency-domain method is developed for calculation of sound propagation through rectangular ducts. The goal is to perform numerical simulations for a flow-impedance tube to provide the time-domain method of Özyörük and Long with benchmarking data. The frequency-domain method is based on a transformation of the time-dependent linearized Euler equations into frequency-domain equations and a consequent pseudo time–marching solution of them using a four-stage Runge-Kutta scheme. Frequency-domain simulations are performed at the same flow and frequency conditions as the time-domain simulations. Results are compared with those of the time-domain method and experimental data at various

frequencies and flow conditions. Frequency-domain calculations show very good agreement with the time-domain calculations and experimental data.

Keywords: Sound propagation, Flow-impedance tube, Impedance condition, Finite difference, Nonreflecting boundary conditions

ÖZ

AKUSTİK EMİCİLİ AKIŞ TAŞIYAN KANALLARDA SESİN İLERLEMESİNİN FREKANS ALANINDA SİMULASYONU

Şirzai, Ahmet
Yüksek Lisans, Havacılık Mühendisliği Bölümü
Tez Yöneticisi: Doç. Dr. Yusuf Özyörük.

Ağustos 2000, 71 sayfa

Sesin dikdörtgen kanallarda ilerlemesinin incelenmesi için frekans alanında bir yöntem geliştirilmiştir. Amaç, bir akış-empedans tüpünün sayısal simulasyonunu Özyörük ve Long' un zaman alanındaki yöntemini desteklemek için icra etmektir. Frekans alanındaki yöntem, zamana bağlı Euler denklemlerinin frekansa bağlı denklemlere dönüştürülmesine ve dört safhalı Runge-Kutta metodunu kullanarak denklemlerin suni olarak zamana bağlı bir çözüme dayanmaktadır. Frekans alanındaki simulasyonlar zaman alanındaki simulasyonlarla aynı akış ve frekans şartlarında icra edilmiştir. Sonuçlar, zaman alanındaki yöntemin sonuçları ve deneysel verilerle değişik frekans ve akış şartlarında karşılaştırılmıştır. Frekans

alanındaki sonuçlar, zaman alanındaki sonuçlar ve deneysel verilerle çok iyi uyum göstermiştir.

Anahtar Kelimeler: Sesin ilerlemesi, Akış-empedans tüpü, Empedans şartı, Sonlu fark, Yansımayan sınır şartları.

To My Parents

ACKNOWLEDGMENTS

I express sincere appreciation to Assoc. Prof. Dr. Yusuf Özyörük for his guidance, insight and encouragement throughout the research. I offer sincere thanks to all department members for their suggestions and support during the graduate education. I would like to express my sincere thanks to Turkish Air Force for giving me the permission to achieve graduate education. I offer my sincere thanks to my wife, Hülya, for her patience.

TABLE OF CONTENTS

LIST OF TABLES

TABLE

LIST OF FIGURES

FIGURES

LIST OF SYMBOLS

SYMBOLS

c_0	speed of sound in the acoustic medium
f	frequency
k_x, k_y	wavenumber
M_{pk}	mean-flow centerline Mach number
$\mathbf{n}$	inward surface normal
p'_{ref}	reference pressure (20 μPa)
p'_{rms}	root mean square of perturbed pressure
$p_0, \rho_0, \mathbf{V}_0$	mean pressure, density and velocity
R	resistance of surface
SPL	sound pressure level
t	time
u', v', p'	velocity and pressure perturbations
$\hat{u}, \hat{v}, \hat{p}$	complex amplitudes of perturbed quantities
X	reactance of surface
$\boldsymbol{x}_s, \boldsymbol{x}, \boldsymbol{y}$	coordinate vectors
Z	specific acoustic impedance
ω	angular frequency ($2\pi f$)
λ	eigenvalue

CHAPTER 1

INTRODUCTION

1.1 Sources of Noise

Acoustics is the science of sound, including its production, transmission, and physical effects on substances and bodies with which it interacts [1]. Sound is a pressure disturbance in atmosphere. Such disturbances are produced by practically everything that moves, especially if it moves in a rapid and repetitive manner. If we could make such a disturbance visible somehow, we could see the disturbance lines, which are called wavefronts, like waves caused by a stone dropped into a water pond. Sound propagation is defined as the transmission of acoustic energy through a medium via a sound wave. Sound that might be enjoyable to some people will be intolerable to others, depending upon a person's interests, activity, and mood. Some type of sound sensation is usually unwanted, assuming the sound intensity is at high level; thus, any unwanted sound is often referred to as noise.

Noise may be associated with every type of human activity, and it is emitted from almost all apparatus having moving components. Machinery, office equipment, fans, ducts, gears and bearings, plumbing, traffic, engines, airplane all generate a spectrum of noise. Electrical equipments may also be a significant noise source. Therefore, noise is one of the major problems in engineering design, which might

influence our health, performance, and comfort. For example, aircraft noise is a crucial problem for people who live near airports. In these regions, high levels of noise can create an environment that is unpleasant for work, sleep, and recreation. High levels of noise can even result in permanent hearing loss, physiological and mental problems. The reason for this can be given as the increasing volume of air traffic and turbofan-powered airplanes that result in unacceptable noise exposures. Since fan noise is extremely important problem for turbofan-powered commercial aircraft on landing approach as well as takeoff, Federal Aviation Rules were set for maximum takeoff, landing, and sideline noise levels for certification of airplanes [2,3]. For these reasons, determination of the noise sources and reduction of the noise emitting from airplanes are required.

Acoustics has applications in many fields, such as architectural acoustics, electroacoustics, duct acoustics, and aeroacoustics. Many noise sources are found in dealing with aeroacoustics of airvehicles. Some of these are, for example, airframe noise, turbomachinery (engine) noise, and jet noise on an airplane; blade vortex interaction (BVI) noise, shock noise, and tail rotor noise on a helicopter [3,4]. There are many parameters that affect production and transmission of all these types of noise. For example, the blade shape, number of rotor blades and blade tip velocity are some important parameters affecting helicopter noise. A schematic illustration of some important noise sources on an airplane is shown in Fig. 1.1. Shown are the gears, flaps, slats, fuselage, wing, empennage, boundary layer, and horizontal tail as noise sources.

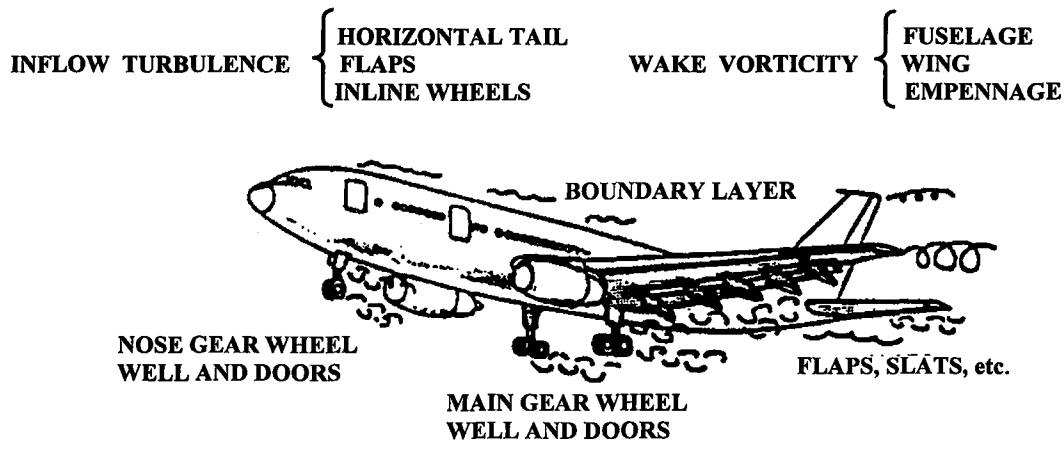

Figure 1.1 Schematic illustration of airframe noise

Noise sources from an aircraft engine can be identified as rotor-stator (fan, compressor, turbine) interaction noise, combustion noise, boundary layer noise, mechanical vibration noise, free-stream turbulence-fan interaction noise, and jet noise. High-speed turbomachines produce a great deal of rotor-stator interaction noise. On takeoff, the jet noise is dominant; for subsonic high-bypass turbofan engines, fan-exhaust noise and fan-inlet noise are critical during both takeoff and approach [2]. A schematic illustration of noise sources from a subsonic turbofan engine is given in Fig. 1.2.

To control unwanted sound emitting from an environment, two methods are used. These are active control and passive control [4,5]. Sound field is modified, and even sound cancellation is created in active control for suppressing noise. But active control is complicated and expensive. Passive techniques work best and are important to nearly all products in today's increasingly noise-sensitive world. Passive noise control treatments include silencers, vibration mounts, damping treatments, absorptive treatments, such as acoustic treatment panels.

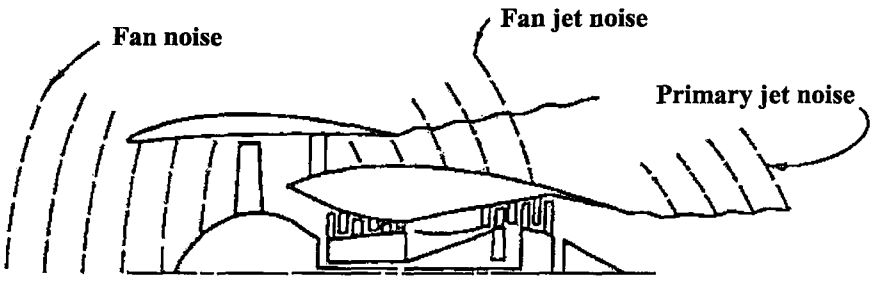

Figure 1.2 Schematic illustration of noise sources from a subsonic turbofan engine

1.2 Acoustic Treatment Panels (Liners)

There are several important factors, which affect propagation of sound in a medium. One of these is the surface effect. If sound is propagating over a surface, attenuation will occur due to acoustic energy losses on reflection, absorption, and transmission [1,6]. Levels of these losses depend on the type of the surface. Surfaces are separated into two acoustic groups; the first group includes hard surfaces (structural surfaces), and the second group includes soft surfaces (acoustically treated surfaces or penetrable surfaces), which allow passage of incoming and outgoing acoustic waves across the surface.

A quantity, which is used to determine the acoustic character of a surface, as hard or soft, is the specific acoustic impedance. The ratio

$$Z(\omega, \boldsymbol{x}_s) = \frac{\hat{p}(\omega, \boldsymbol{x}_s)}{\hat{v}_n(\omega, \boldsymbol{x}_s)} \tag{1}$$

defines the specific acoustic impedance Z of a surface, where $\hat{p}$ is the complex amplitude of the pressure perturbation at surface point $\boldsymbol{x}_s$ and $\hat{v}_n$ is the complex amplitude of the normal velocity perturbation at the same point (a solution variable $\hat{q}(\omega, \boldsymbol{x})$ can be viewed as the Fourier transform of $q'(t, \boldsymbol{x})$), and ω is the circular

frequency of the acoustic wave. The normal velocity perturbation is positive when it points into the surface [1]. If a surface is acoustically rigid, the complex amplitude of the normal velocity perturbation $\hat{v}_n$ will be zero on the surface. In other words, acoustically rigid surfaces have zero specific acoustic admittance, which is defined as $1/Z$. By analogy to electrical impedance, the specific acoustic impedance is defined as

$$Z(\omega) = R(\omega) + i\,X(\omega) \tag{2}$$

where $R(\omega)$ and $X(\omega)$ are the resistance and reactance, respectively, of the acoustic treatment panel, and $i = \sqrt{-1}$. It is clear that the impedance is a frequency-dependent complex quantity. The acoustic resistance R of a surface is the real component of the acoustic impedance that is associated with the absorption of acoustic energy. Similarly, the acoustic reactance X of a surface is the imaginary component of the acoustic impedance that results from the pressure difference caused by influx and efflux of the gas through an acoustic element. The acoustic resistance R analogous to the electrical resistance, and the acoustic reactance X analogous to the electrical inductance and capacitance [7].

Absorption means the loss or dissipation of sound energy in passing through a material or on striking of a surface [5]. Absorption of acoustic energy by high impedance materials (hard surfaces) is less than by low impedance materials (soft surfaces). Because of this property, acoustic treatment panels (liners) have been used as sound absorbers in architectural design and industrial installations. For different applications and purposes, liners are made up from various materials with different structural properties. For example, liners used in the interior of a jet engine should have minimum thickness and weight, should be able to resist high-pressure levels,

face extreme temperature differences, and of course should have sufficient ability to absorb sound. These liners are usually made up of porous or perforated plates, and honeycomb core [8]. Various types of liners are shown schematically in Fig 1.3.

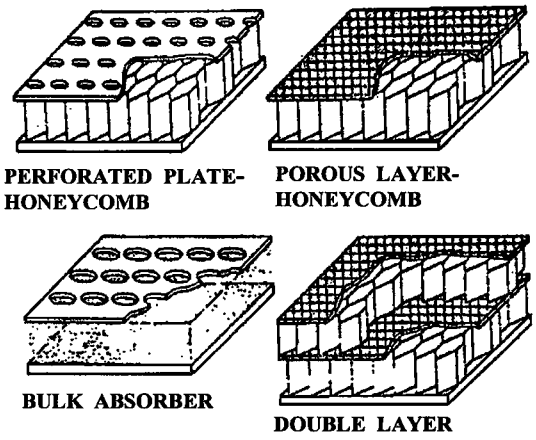

Figure 1.3 Schematic of various lining type

Since the impedance of a liner is different from the impedance of the incident sound field, liner attenuates some of the acoustic modes and reflects the rest as illustrated in Fig. 1.4. The physical law for reflection of sound from a surface is similar to that for light.

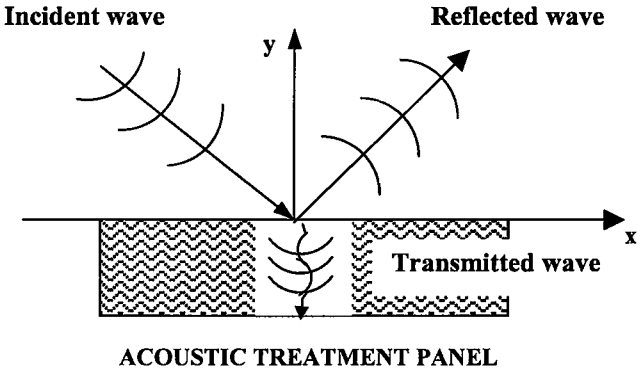

Figure 1.4 Reflection and transmission of incident sound wave

Liners usually consist of a large number of cavities, as in Helmholtz resonators. A simple Helmholtz resonator is a hollow sphere or a cavity with a small opening.

Schematic of a typical treatment panel is shown in Fig. 1.5. Such a resonator consists of a rigid enclosure of volume, communicating with the external medium through a small opening. The pressure of the gas within the cavity changes as it is alternately compressed and expanded by the mass addition into the cavity and mass extraction from the cavity through the opening. This results in fluctuations, radiation of sound into the surrounding medium, and vortex shedding at the mouth of the cavity. This in turn leads to absorption of acoustic energy [7].

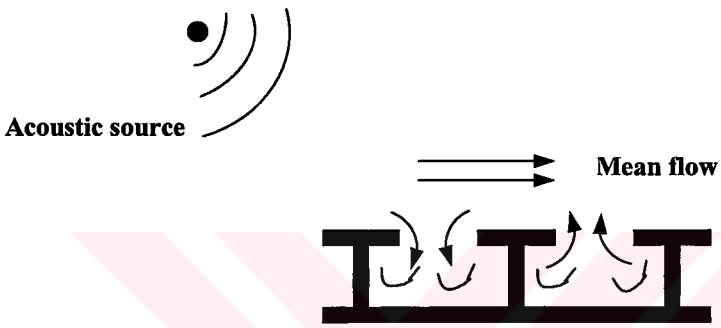

Figure 1.5 Schematic of a typical treatment panel

The specific acoustic impedance (resistance and reactance) varies with incident sound waves and adjacent mean flow velocity that directly influence the sound absorption ability of liners [9]. This depends on the intensity and propagation direction of the incident sound waves. Any existing airflow with velocity gradients and boundary layers produces a refraction of sound wave away or toward the liner. Airflow changes the intensity of incident sound waves because of the convective effects of the flow, which might also cause refraction of sound waves.

The specific acoustic impedance also depends on the angle of incidence that is the angle between the propagation direction and the surface normal, and moreover,

depends on the spatial distribution of the wave causing the pressure [1]. Thus the motion of fluid at one point is related to motion at another point of the surface, the relationship being determined by the wave motion inside the acoustic material, as well as by the incident and reflected waves. In most cases the effects of the surrounding on a surface are neglected because various parts of the surface are not strongly coupled together. Sometimes at every point on such a surface the specific acoustic impedance may be considered fixed; thus, the acoustic normal velocity at a given point is determined by the acoustic pressure at the same point, $\hat{p} = Z\hat{v}_n$. In such cases the treatment panel is said to have a locally reacting surface [1,6,10]. Locally reacting liners permit propagation only in the direction normal to the surface. Such liners are the most common in practice because they are easy to manufacture and possess desirable structural properties [8]. They are usually made up of perforated plates, porous plates, and honeycomb core as shown in Fig. 1.3.

1.3 Background to the Study

Future aircraft engines are expected to have ultrahigh bypass ratios to achieve lower specific fuel consumption. This results in a reduction of the jet noise to relatively insignificant levels, but also results in an increase of the fan noise [8]. This is part of why noise levels must be held under a standard level near airports. This indicates that parallel to developments in technology, reduction of emission of noise from commercial airplane is necessary to meet noise regulations.

In an engine duct, the interaction between flow and the moving blades produces upstream and downstream travelling pressure waves (acoustic modes), such as fan-inlet and fan exhaust noise, as shown in Fig. 1.2. Some of these modes

decay naturally, and acoustic treatment is invariably used on the inside surface of all such engines to suppress the others [8,9]. Schematic of usage of liner in a turbofan engine is shown in Fig.1.6.

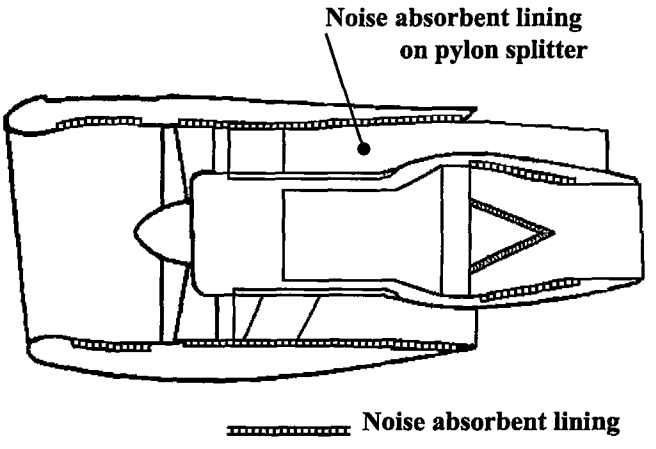

Figure 1.6 Schematic illustration of usage of liners in a turbofan engine

To be able to use an acoustic material in an environment, accurate determination of the impedance properties of the material is required [8,11]. For this reason, flow impedance tubes are used for testing designed materials. However, designing and testing procedure is usually expensive, laborious, and time consuming. This is a continuing measurement problem in treatment technology. Understanding problems and solving them in a quick and efficient manner is necessary. Therefore, numerical simulations are used to analyze sound propagation in lined ducts.

In the literature, various methods have been developed to simulate sound propagation in a lined duct. The behavior of the acoustic treatment panels is frequency dependent. In addition, an acoustic impedance condition was established for frequency-domain analyses [12]. For this reason, until the recent years, many

methods had been developed in frequency domain for simulations of sound propagation in acoustically treated ducts, and for extraction of the impedance property of the acoustic material. Unruh and Eversman [13] applied the Galerkin method for sound propagation in acoustically treated ducts with a sheared flow profile of two spatial variables. Their analyses were on the symmetric configuration of a rectangular duct with two walls lined and two walls hard. They validated the applicability of the Galerkin method to the solution of an acoustic sheared flow problem [13]. Watson et al. [14,15] developed a method without mean flow using a propagation model based upon a finite element technique for extracting the acoustic impedance of a test specimen from measured wall pressure data. In their studies, simulations were performed in two dimensions using the Helmholtz equation.

In recent years, time-domain methods have been developed because of their certain advantages over frequency domain methods. One significant advantage of time-domain methods is that broadband (multifrequency) noise problems can be handled easily; many frequencies can be run at once unlike frequency-domain methods. For broadband noise problems, frequency-domain methods are computationally intensive and laborious [9]. Another significant advantage of time-domain methods is the ability to treat nonlinear effects [16]. Nonlinear effects play an important role in sound attenuation at high sound pressure levels (above 130 dB). These nonlinear effects can be considered as the nonlinearity of the gas itself and the nonlinearity of the acoustic properties of the lining material that depend on the sound frequency [8]. Besides these advantages, in order to model acoustically treated walls in computational aeroacoustics (CAA) applications, appropriate

modeling of the impedance condition in time domain is required; therefore, work was done for developing an appropriate time-domain impedance condition [9,17].

As mentioned in reference [17], the application of the impedance condition is extremely difficult, because a direct time domain approach involves convolutions. Therefore, Özyörük and Long [17] developed a time-domain method to overcome the computational difficulties associated with convolutions. Their method was based on the z-transform and its time-shifting and convolution properties. They used the z-transform to formulate the impedance condition in time domain in order to apply the impedance condition in a numerical algorithm. They applied their method to one- and two-dimensional example problems with and without flow, and showed excellent agreement between the computed and exact solutions for one-dimensional wave propagation. The developed time-domain impedance condition [17] was validated by Özyörük et al.[11] solving an actual engineering problem. They performed time-domain numerical simulations of a flow-impedance tube at various frequencies with and without flow (uniform flow). They obtained good agreement between the simulated results and experimental data. However, they observed some numerical instabilities at some conditions, which were caused by impedance jumps between the hard and soft walls. Including the refraction effects of sheared flows on sound propagation, Özyörük and Long [16] obtained improved results. They concluded that the use of sheared flows allows solutions at high Mach numbers without numerical difficulties, which were encountered in the uniform flow cases.

1.4 Scope and Overview of the Thesis

In the previous subsection, the advantages of the time-domain methods and the requirement for an appropriate impedance condition in time domain for CAA applications were discussed. Appropriate time-domain impedance condition allows the use of the newly developed CAA methods for the solution of turbomachinery noise and duct acoustics problems. However, application of the impedance condition in time domain is difficult, and any implementation is required to be validated. One certain but expensive and time consuming way is experimental validation and another is to simulate the same problem in frequency domain using the same conditions.

Our objective in this study is to simulate sound propagation in a flow impedance tube in frequency space and compare results with those of the time-domain simulations that have been performed previously by Özyörük and Long [16].

Since the time-domain results were obtained for the NASA Langley flow-impedance tube, the present simulations are also performed using the same impedance tube. Two-dimensional schematic of the test section of the flow-impedance tube is given in Fig. 1.7. The test section is 84 cm in length and it has a cross section of 5.08 cm x 5.08 cm. Entire upper wall and a portion of the lower wall are acoustically rigid. An airflow exists and acoustic plane waves propagate from left to right. A liner is placed at the lower part of the tube. A microphone along the upper wall is traversed to measure the sound pressure level (SPL). SPL is defined by

$$\mathrm{SPL} = 20 \log_{10}\left(\frac{P'_{\mathrm{rms}}}{P_{\mathrm{ref}}}\right) \tag{3}$$

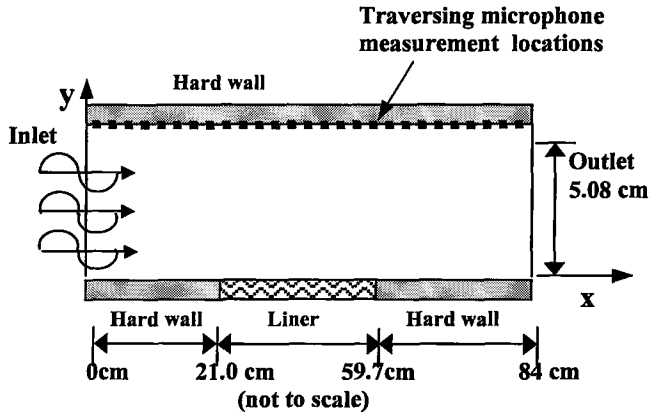

Figure 1.7. Two-dimensional schematic of the test section of a flow-impedance tube

where P'_{rms} is root mean square of perturbed pressure p', and P_{ref} is reference pressure ($P_{ref} = 20$ μPa).

In the thesis, chapters are presented in the following order. In chapter 2, the mathematical model is introduced. The relations between time- and frequency-dependent variables are given, and then, the time-domain equations [16] are transformed into frequency-domain equations. These include the 2D linearized Euler equations, nonreflecting conditions at the inlet and outlet sections, and the wall conditions. In chapter 3, the numerical method used in this study is introduced. In chapter 4, numerical simulations are discussed and results are compared with the time-domain results [16] and also with experimental data [16]. In chapter 5, some conclusions are drawn from this study.

CHAPTER 2

MATHEMATICAL APPROACH

2.1 Governing Equations

As noted in the previous chapter, the problem we study involves acoustic propagation through the NASA Langley flow-impedance tube. This tube has a rectangular cross section and hard side walls (acoustically rigid). The dimensions of its test section are 5.08cm x 5.08cm x 84cm, which is shown schematically in Fig. 1.7. The spanwise direction, normal to the (x,y) plane, is not shown in the figure.

In real situations, the flow in the tube is three-dimensional because of the finite span size of the tube. However, the span of the test section is smaller than the shortest wavelength we consider. Therefore, we expect that spanwise variations in the acoustic field will be insignificant. Also, because of the size of the cross section of the tube, only plane waves are propagated at far distances from the liner, and the other modes are naturally cut-off. Therefore, simulations employ only plane waves, which are introduced at the inlet. Hence, the problem is reduced to two dimensions.

When an acoustic field is present, the fluid state quantities can be stated as a combination of the mean and perturbation quantities. This indicates that acoustic

disturbances can usually be regarded as small-amplitude perturbations to an ambient state (p_0, ρ_0, $\mathbf{V}_0$); that is,

$$\begin{aligned} p &= p_0 + p' \\ \rho &= \rho_0 + \rho' \\ \mathbf{V} &= \mathbf{V}_0 + \mathbf{V}' \end{aligned} \tag{4}$$

where $\mathbf{V}$ is the velocity vector, and p', ρ', $\mathbf{V}'$ are the pressure, density, and velocity perturbations, respectively, and those with a zero subscript indicate the mean quantities. In general, acoustic disturbances in the impedance tube satisfy the compressible, inviscid, linearized equations of motion. Therefore, the two-dimensional linearized Euler equations are used as the governing equations in this study. The Euler equations are a combination of the continuity and inviscid momentum equations without body force. The differential form of the 2D Euler equations are given as

$$\frac{\partial \rho}{\partial t} + \frac{\partial}{\partial x_i} \rho u_i = 0 \tag{5}$$

$$\frac{\partial (\rho u_i)}{\partial t} + \frac{\partial}{\partial x_j} \rho u_i u_j + \frac{\partial p}{\partial x_i} = 0 \tag{6}$$

These equations are linearized about a nonuniform mean flow. In computational domain, no flow penetrates the upper and lower hard walls except on the acoustically treated surface, and it is assumed that flow is unidirectional between the stationary finite parallel walls of the tube. The length of the tube is long enough compared to its height so that the velocity profile does not change with increasing distance in the x-direction. In other words, the mean flow is fully developed. In the Cartesian coordinate system, the velocity (with zero normal component) is given as

$$\mathbf{V}_0 = u_0(y)\,\mathbf{i} + 0\,\mathbf{j} \tag{7}$$

In the linearization process, Eqs.(4) and (7) are substituted into the 2D Euler equations, and then nonlinear terms are neglected with the assumption that perturbations are small compared to mean quantities. In addition to linearization, expanding an important relation, $p = p(\rho)$, between density and pressure for compressible fluid around the mean pressure and neglecting higher order terms result in

$$\frac{p'}{\rho'} = \left(\frac{\partial p}{\partial \rho}\right)_0 = c_0^2 \tag{8}$$

This definition gives the relation between the pressure perturbation, density perturbation and the speed of sound for isentropic acoustic processes. The relation from Eq.(7), $\rho' = p'/c_0^2$, is substituted into the linearized continuity equation, and then the 2D linearized Euler equations take the form

$$\frac{\partial u'}{\partial t} + u_0 \frac{\partial u'}{\partial x} + \frac{1}{\rho_0}\frac{\partial p'}{\partial x} = -v'\frac{\partial u_0}{\partial y} \tag{9}$$

$$\frac{\partial v'}{\partial t} + u_0 \frac{\partial v'}{\partial x} + \frac{1}{\rho_0}\frac{\partial p'}{\partial y} = 0 \tag{10}$$

$$\frac{\partial p'}{\partial x} + u_0 \frac{\partial p'}{\partial x} + \rho_0 c_0^2 \left(\frac{\partial u'}{\partial x} + \frac{\partial v'}{\partial y}\right) = 0 \tag{11}$$

where all perturbation variables are functions of time t and space $\boldsymbol{x}$.

Our objective here is to simulate wave propagation in frequency domain and compare the results with those of the time-domain simulations that have been performed previously [16]. For this reason, it is required to transform the above time-domain equations into frequency domain. Firstly, it is needed to define the relations between the time- and frequency-dependent variables.

An acoustic disturbance is of constant frequency if the field variables oscillate sinusoidally with time about a mean flow, such that the acoustic pressure oscillates with time t as

$$p'(t, \boldsymbol{x}) = P_{\text{pk}} \cos(\omega t + \phi_{\text{c}}) = P_{\text{pk}} \sin(\omega t + \phi_{\text{s}}) \tag{12}$$

where P_{pk} is peak value of the pressure perturbation, ω is the angular frequency, ϕ is the phase, t is time, and $\boldsymbol{x}$ is the position vector. Such disturbances have the same repetition period at every point, but generally, the phase varies from point to point. If an acoustic disturbance oscillates with a constant frequency or one frequency component of a multifrequency, it is convenient to use a complex representation [2], such that acoustic variables are written as

$$\begin{aligned} p'(t, \boldsymbol{x}) &= \text{Re}\ \{\, \hat{p}\,(\omega, \boldsymbol{x})\, \text{e}^{i\omega t} \} \\ u'(t, \boldsymbol{x}) &= \text{Re}\ \{\, \hat{u}\,(\omega, \boldsymbol{x})\, \text{e}^{i\omega t} \} \\ v'(t, \boldsymbol{x}) &= \text{Re}\ \{\, \hat{v}\,(\omega, \boldsymbol{x})\, \text{e}^{i\omega t} \} \end{aligned} \tag{13}$$

where $\hat{p}$, $\hat{u}$, $\hat{v}$ are complex amplitudes of the perturbed quantities, $i = \sqrt{-1}$, and Re signifies the real part of a complex variable. As is clear from Eq.(13), the complex amplitudes depend only on frequency and space. Hence, all the time-domain equations are transformed into frequency-domain equations replacing all the field variables by their complex amplitudes and all the time derivative operators with $i\omega$, that is, $\partial/\partial t \Rightarrow i\omega$. Thus, in frequency domain the 2D linearized Euler equations are written as

$$i\omega\hat{u} + u_0 \frac{\partial \hat{u}}{\partial x} + \frac{1}{\rho_0} \frac{\partial \hat{p}}{\partial x} = -\hat{v} \frac{\partial u_0}{\partial y} \tag{14}$$

$$i\omega\hat{v} + u_0 \frac{\partial \hat{v}}{\partial x} + \frac{1}{\rho_0} \frac{\partial \hat{p}}{\partial y} = 0 \tag{15}$$

$$i\omega\hat{p} + u_0 \frac{\partial \hat{p}}{\partial x} + \rho_0 c_0^2 \left(\frac{\partial \hat{u}}{\partial x} + \frac{\partial \hat{v}}{\partial y} \right) = 0 \tag{16}$$

where ρ_0 is the mean density, p_0 is the mean pressure, c_0 is the speed of the sound and ρ_0, p_0, c_0 are all uniform in the tube.

2.2 Boundary Conditions

The schematic of the test section of the flow-impedance tube was shown in Fig. 1.7. The two ends of the tube are open, and an acoustic source is placed at the inlet section (left-hand side). Airflow is from left to right as well as the sound propagation. The entire upper wall and a portion of the lower wall are acoustically rigid (zero admittance). An acoustic treatment panel is placed on the lower wall of the tube. All of these form the physical boundaries of the computational domain. The values of the dependent variables at the boundaries must be determined as a part of the overall solution, because a small variation at these boundaries gives rise to a small variation in the solution at any point in the domain. Specifications of the boundary conditions depend on the problem.

In this study, we need four boundary conditions: Hard wall conditions are applied on acoustically rigid surfaces because of the vanishing normal velocity. On the acoustic treatment panel, an impedance boundary condition is required since there is fluid penetration into the wall. The inlet and outlet boundaries of the domain are free artificial boundaries. Therefore, there must not be reflections from these boundaries. This is accomplished applying characteristics based boundary conditions at these sections.

2.2.1 Nonreflecting Boundary Conditions

Since the solution in the computational domain may be affected by reflections at inlet and outlet sections, reflections are unwanted at these boundaries. To prevent spurious, nonphysical reflections, a long computational domain is needed to minimize the effects of reflected waves. This is often impractical. Instead, nonreflecting boundary conditions are used with a relatively short domain.

Time-dependent nonreflecting boundary conditions for Euler equation calculations were derived by Giles [18], and they were used by Özyörük et al. [11]. Özyörük and Long [19] used Thompson's time-dependent boundary conditions [20] given for the nonlinear Euler equations applying linearization about a nonuniform background flow. An advantage of these conditions is that calculations can be performed on a much smaller computational domain with sufficient mesh resolution [16]. These conditions were tested to assess whether or not they worked accurately in time-domain simulations of the flow impedance tube [11,16,19]. In these studies, a standard computational domain was defined with inlet and outlet sections located at $x = 0$ cm and $x = 84$ cm, respectively. The domain was also arbitrarily extended to upstream (from $x =$ -15.7 cm to 84 cm), and to downstream (from $x = 0$ cm to 106.3 cm) to form two relatively long domains. A short domain (from $x = 0$ cm to 63.2 cm) was also used to test the inlet and outlet boundary conditions. Comparisons of the results indicated the inlet and outlet boundary conditions worked well.

Time-dependent nonreflecting inlet and outlet boundary conditions were given in the characteristics form, which are given for the 2D linearized Euler equations as

$$
\begin{aligned}
c_1 &= p' - c_0^2 \rho' \quad , \\
c_2 &= \rho_0 c_0 v' \quad , \\
c_3 &= p' + \rho_0 c_0 u' \quad , \\
c_4 &= p' - \rho_0 c_0 u' \quad ,
\end{aligned} \tag{17}
$$

where c_1, c_2, c_3, and c_4 correspond to entropy waves, vorticity waves, downstream propagating acoustic pressure waves, and upstream propagating acoustic pressure waves, respectively. Boundary conditions are solved for these characteristic quantities and the dependent perturbations are found from these characteristics by inversion.

These characteristics express that in general, any disturbances governed by inviscid, linearized equations without heat transfer is considered as a superposition of vorticity, entropy, and acoustic modal wave fields [1]. Acoustic mode refers to upstream and downstream running pressure waves. Any perturbed quantity q' is given in the form

$$
q' = q'_{\text{vor}} + q'_{\text{ent}} + q'_{\text{ac}} \tag{18}
$$

The individual modal wave fields satisfy the Euler equations. Linear acoustics is primarily concerned with solutions of the equations that govern the acoustic modes, while conduction of heat transfer is primarily concerned with solutions of the equations that govern the entropy mode. However, all three modes are often required simultaneously in some cases such as acoustic boundary layer problems. The relations between boundary conditions and modal wave fields will be explained in the next subsections.

2.2.1.1 Inlet Conditions

Characteristics based nonreflecting boundary conditions [18,20] are used at the inlet section. These conditions allow the incoming and outgoing waves to pass the inlet boundary without reflection. A source term in the equations generates incoming acoustic plane waves at desired frequency and sound pressure levels (SPL). As will be explained later, the acoustic treatment panel generates additional modes that propagate in both directions in the duct [6,19]. Upstream propagating acoustic pressure waves, c_4 , are allowed to pass the boundary without reflection. Vorticity waves, c_2 , are not allowed to penetrate into the computational domain. Hence, the inlet conditions are given as

$$i\omega\hat{u} - (\frac{u_0 - c_0}{2\rho_0 c_0})\frac{\partial}{\partial x}(\hat{p} - \rho_0 c_0 \hat{u}) + (\frac{c_0 - u_0}{4} - \frac{c_0}{2})\frac{\partial \hat{v}}{\partial y} + \hat{v}\frac{\partial u_0}{\partial y} = -\frac{1}{2\rho_0 c_0}\hat{L}_5 \quad (19)$$

$$i\omega\hat{v} + \frac{1}{\rho_0}\frac{\partial \hat{p}}{\partial y} = 0 \quad (20)$$

$$i\omega\hat{p} + (\frac{u_0 - c_0}{2})\frac{\partial}{\partial x}(\hat{p} - \rho_0 c_0 \hat{u}) + (\frac{c_0 - u_0}{4} + \frac{c_0}{2})\rho_0 c_0 \frac{\partial \hat{v}}{\partial y} = -\frac{1}{2}\hat{L}_5 \quad (21)$$

where the source term $\hat{L}_5$ is given as

$$\hat{L}_5 = -2\sqrt{2}\, p_{\text{ref}}\, 10^{A/20}\, i\omega\, e^{i\phi} \quad (22)$$

where p_{ref} is reference pressure, $i = \sqrt{-1}$, ω is circular frequency, ϕ is phase, and SPL is sound pressure level. This source term generates plane waves at a SPL of A db.

2.2.1.2 Outlet Conditions

Nonreflecting boundary conditions are used at the outlet section. However, it was indicated in references [11,21,22] that there were in fact reflections at

downstream sections of the duct, but these reflections were small. This result was revealed by measuring the real and imaginary component of impedance of the medium at downstream locations of the duct [21]. Nonreflecting conditions allow the downstream propagating acoustic pressure waves, c_3, to pass the outlet boundary without reflection and do not allow incoming acoustic waves into the computational domain. Vorticity waves, c_2, pass the boundary without reflection. Hence, the outlet conditions are given as

$$i\omega\hat{u} + \left(\frac{u_0 + c_0}{2\rho_0 c_0}\right)\frac{\partial}{\partial x}(\hat{p} + \rho_0 c_0 \hat{u}) + \hat{v}\frac{\partial u_0}{\partial y} = 0 \tag{23}$$

$$i\omega\hat{v} + u_0\frac{\partial\hat{v}}{\partial x} + \frac{1}{\rho_0}\frac{\partial\hat{p}}{\partial y} = 0 \tag{24}$$

$$i\omega\hat{p} + \left(\frac{u_0 + c_0}{2}\right)\frac{\partial}{\partial x}(\hat{p} + \rho_0 c_0 \hat{u}) + \rho_0 c_0^2\frac{\partial\hat{v}}{\partial y} = 0 \tag{25}$$

2.2.2 Hard-Wall Conditions

Hard-wall conditions are applied on acoustically rigid surfaces (zero admittance). The entire upper wall and a portion of the lower wall of the flow-impedance tube are acoustically rigid. At an acoustically hard wall normal component of the velocity is zero because no flow penetrates the hard wall, but no restriction is placed on the tangential component of the velocity. Although, in this study, the background flow is sheared and the mean flow velocity is zero at the wall, hard-wall conditions allow fluid particles to slip on the walls. The hard-wall conditions are given as

$$i\omega\hat{u} + u_0\frac{\partial\hat{u}}{\partial x} + \frac{1}{\rho_0}\frac{\partial\hat{p}}{\partial x} = 0 \tag{26}$$

$$i\omega\hat{v} + u_0\frac{\partial\hat{v}}{\partial x} = 0 \tag{27}$$

$$i\omega\hat{p} + u_0\frac{\partial\hat{p}}{\partial x} + \rho_0 c_0^2\left(\frac{\partial\hat{u}}{\partial x} + \frac{\partial\hat{v}}{\partial y}\right) + S c_0\frac{\partial\hat{p}}{\partial y} = 0 \tag{28}$$

where $S = 1$ for upper wall and $S = -1$ for lower wall. Vanishing normal pressure gradient condition is explicitly applied at the corners of the inlet boundary and walls as well as the corners of the outlet and walls.

2.2.3 Impedance Condition

The acoustic impedance condition is applied on the acoustic treatment panel. The general form of the frequency-domain impedance condition was derived by Myers [12]. This condition satisfies the continuity of acoustic particle displacement. It means that acoustically treated surface is acoustically deformed in response to an incident acoustic field or generates perturbations by small deformation. In addition to these, displacement of the acoustic fluid particle is the same as the displacement of the surface boundary itself in the normal direction. The frequency-domain impedance condition linearized about mean flow [11] is given as

$$\begin{aligned} i\omega\,\hat{p}\,(\omega, \boldsymbol{x}) + \mathbf{V}_0(\boldsymbol{x}) \cdot \nabla\,\hat{p}\,(\omega, \boldsymbol{x}) - \mathbf{n} \cdot [\mathbf{n} \cdot \nabla\,\mathbf{V}_0(\boldsymbol{x})]\;\hat{p}\,(\omega, \boldsymbol{x}) \\ = -[\,i\omega\,Z(\omega)\,][\,\mathbf{n} \cdot \hat{\mathbf{V}}\,(\omega, \boldsymbol{x})\,] \end{aligned} \tag{29}$$

where $\hat{p}$ is the complex amplitude of the pressure perturbation, $\mathbf{V}_0$ is the mean velocity, ω is the circular frequency, $\hat{\mathbf{V}}$ is the complex amplitude of the velocity perturbation , $\mathbf{n}$ is the mean surface normal, $i = \sqrt{-1}$, and Z is the impedance. The minus sign at the right-hand side means that surface normal is out of the surface.

Impedance depends on the frequency of the incident wave at a point on the surface. But the acoustically treated surface is assumed as locally reacting [11,18]; thus, the effects of surrounding on the behavior of the treatment panel are neglected. That is, the impedance does not depend on the spatial distribution of the wave causing the pressure. Hence, we apply the same condition on the entire impedance

surface. If nonuniform mean flow velocity given by Eq.(7) is placed into the impedance condition, the condition used in this study on acoustic treatment panel becomes

$$i\omega \hat{p} + u_0 \frac{\partial \hat{p}}{\partial x} = -(i\omega Z)\hat{v} \tag{30}$$

where the complex amplitude of the normal velocity perturbation is not zero. Since none of the velocity components is zero on impedance wall, we need some extra equations to solve the problem. We use the momentum equations. Then the following equations are solved on the acoustic treatment panel.

$$i\omega \hat{u} + u_0 \frac{\partial \hat{u}}{\partial x} + \frac{1}{\rho_0}\frac{\partial \hat{p}}{\partial x} = -\hat{v}\frac{\partial u_0}{\partial y} \tag{31}$$

$$i\omega \hat{v} + u_0 \frac{\partial \hat{v}}{\partial x} + \frac{1}{\rho_0}\frac{\partial \hat{p}}{\partial y} = 0 \tag{32}$$

$$i\omega \hat{p} + u_0 \frac{\partial \hat{p}}{\partial x} = -(i\omega Z)\hat{v} \tag{33}$$

CHAPTER 3

NUMERICAL IMPLEMENTATION

3.1 Grid System

Because of the two-dimensional approach that we are using and the rectangular cross section of the flow-impedance tube, two-dimensional Cartesian meshes are used in the simulations. The physical dimension of the computational domain is 84cm x 5.08cm. Flow and sound propagation directions are from left to right. Therefore, location (x = 0, y = 0) at the inlet indicates grid point (1,1) as shown in Fig. 3.1. The number of maximum grid points is denoted N_y in the y-direction and N_x in the x-direction. The Grid size is adjusted according to the flow Mach number and the wave frequency to get sufficient resolution [16]. An important parameter in the determination of the grid size is the number of grid points per wavelength (wavelength / grid spacing).

As pointed out earlier, fluid particles penetrate an impedance wall. Therefore, to handle the effects of inside variables and for proper discretization of the boundary conditions we use ghost grid points inside the wall. Upper and lower walls are placed midway between two grid points as shown in Fig. 3.1. It should be noted that microphones are placed along the upper wall to measure acoustic pressure. Each grid point on the upper wall represents a microphone position. Having obtained

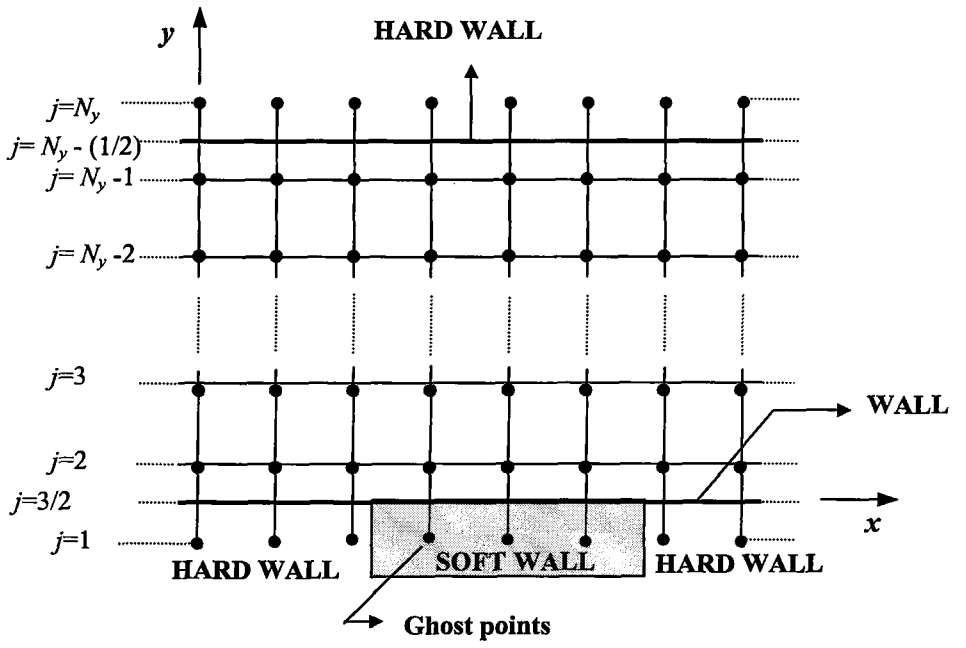

Figure 3.1 Spatial discretization at and near the wall

the results at the ghost points, an interpolation formula, as explained in the next section, is used to find the acoustic pressure on the wall.

3.2 Discretization of Equations

3.2.1 Spatial Discretization

Finite differences are used to discretize the governing equations. These equations are first-order partial differential equations in space and are time-independent. In discretization, a distinct order of accuracy is used depending upon the location of the grid point. The fourth-order accurate central difference formula is employed in the interior region and biased differences are used at and near the boundaries [16]. The finite difference formulas that are used in this study are given in Appendix A. These finite difference formulas show the discretizations of the

equations at and near the wall using the ghost point quantities inside the wall. Any quantity at the wall is found by a fourth-order interpolation formula [11], which is

$$q_{i,\frac{3}{2}} = \frac{5q_{i,1} + 15q_{i,2} - 5q_{i,3} + q_{i,4}}{16} \tag{34}$$

$$q_{i,N_y-\frac{1}{2}} = \frac{5q_{i,N_y} + 15q_{i,N_y-1} - 5q_{i,N_y-2} + q_{i,N_y-3}}{16} \tag{35}$$

where $q_{i,1}$ and q_{i,N_y} are the ghost point quantities. The above interpolation formulas are inserted into the discretized equations (at points j = 3/2 and $j = N_y$ -(1/2)), instead of using the wall quantities.

3.2.2 Pseudo Time-Marching

Our first attempt for the solution of the flow-impedance tube problem was to use a direct method. Eqs.(14), (15), and (16) and boundary conditions Eqs.(19-33) were discretized directly. This resulted in a linear system of equations. Since there are three unknowns and three discretized equations at each grid point, the size of the linear system equations was NxN, where $N = 3N_xN_y$ with N_x and N_y being the number of grid points in the x- and y-directions, respectively. It should be noted that all variables are complex. The complex system is separated into real and imaginary parts. Then a set of 2Nx2N equations is obtained with real arithmetic. For example, a 71x14 computational mesh requires a 5964x5964 linear set. Because of such an excessive number of matrix elements, we encountered memory problems on the available computers to us. A grid of 71x14, for example, required about 256 Mb ram in double-precision and about 2 hours of CPU time on a Pentium II processor. Although the direct method was a simple and an accurate method, working with

such a large linear system of equations caused excessive computational cost and memory requirement.

From this point of view, pseudo-time-marching of the equations is considered for an explicit solution of the equations, reducing the computational cost and memory requirement. A time derivative is added to the steady-state equations, and the four-stage compact Runge-Kutta (R-K) scheme is used. Some more stable methods also exist, but the R-K method has some advantages [23]. It is a simple method for numerical applications. It is capable of handling solutions of both the exponential and oscillatory types of problems with great ease. Its disadvantages are that it requires a large number of function evaluations, and sometimes depending on the step size goes unstable by producing exponential growth rather than decay.

An artificial time derivative is introduced into the governing equations and boundary conditions, so that the R-K scheme can be used to integrate the equations. In addition, fourth-order artificial dissipation $D(\mathbf{Q})$ is added to the linear system of equations for augmenting the scheme, i.e. for dissipating spurious oscillations, such that

$$\frac{d\mathbf{Q}}{dt} = -[\,H(\mathbf{Q}) - D(\mathbf{Q})\,]\ , \tag{36}$$

where

$$H(\mathbf{Q}) = i\omega\,\mathbf{Q} + A\frac{\partial \mathbf{Q}}{\partial \mathrm{x}} + B\frac{\partial \mathbf{Q}}{\partial \mathrm{y}} + C\mathbf{Q} + E \tag{37}$$

in which $\mathbf{Q}$ is the vector of dependent variables $(\hat{u}, \hat{v}, \hat{p}\,)$, $H(\mathbf{Q})$ is collection of the spatial derivatives, A,B,C,E are coefficient matrices, and $D(\mathbf{Q})$ is artificial dissipation.

The four-stage compact Runge-Kutta scheme is given as

$$\begin{aligned}
\mathbf{Q}^{(0)} &= \mathbf{Q}^{n} \\
\mathbf{Q}^{(1)} &= \mathbf{Q}^{n} - \alpha_1 \Delta t \, [\, H(\mathbf{Q}^{(0)}) - D(\mathbf{Q}^{(0)}) \,] \\
\mathbf{Q}^{(2)} &= \mathbf{Q}^{n} - \alpha_2 \Delta t \, [\, H(\mathbf{Q}^{(1)}) - D(\mathbf{Q}^{(0)}) \,] \\
\mathbf{Q}^{(3)} &= \mathbf{Q}^{n} - \alpha_3 \Delta t \, [\, H(\mathbf{Q}^{(2)}) - D(\mathbf{Q}^{(0)}) \,] \\
\mathbf{Q}^{(4)} &= \mathbf{Q}^{n} - \alpha_4 \Delta t \, [\, H(\mathbf{Q}^{(3)}) - D(\mathbf{Q}^{(0)}) \,] \\
\mathbf{Q}^{n+1} &= \mathbf{Q}^{(4)}
\end{aligned} \tag{38}$$

where $\alpha_1 = 1/4$, $\alpha_2 = 1/3$, $\alpha_3 = 1/2$, $\alpha_4 = 1$, and n is the pseudo time-marching step and Δt is the time increment used to advance the solution toward a steady state. The time increment Δt is determined by the stability criteria of the scheme (a Courant number CFL [11]). The CFL number is defined as

$$\mathrm{CFL} = \Delta t \, [\, \frac{u_0 + c_0}{\Delta x} + \frac{c_0}{\Delta y} \,] \tag{39}$$

CFL = 1 is used in the calculations. While $H(\mathbf{Q})$ is updated at every R-K stage, the $D(\mathbf{Q})$ is calculated using the previous iteration level solutions. With this explicit solution, numerical instability and convergence problems are encountered in some cases. To overcome the problems we update the hard-wall, outlet and impedance boundary conditions implicitly at each iteration level n+1.

On the acoustically treated wall, impedance boundary condition Eq.(33) and normal component of momentum equation Eq.(32) give a relation between acoustic pressure $\hat{p}$ and normal acoustic velocity $\hat{v}$, thus impedance boundary condition is rewritten. If we rearrange the equations with zero mean velocity u_0 at the wall (sheared flow) at the current iteration level n+1, the conditions applied on the acoustically treated wall are

$$i\omega\,\hat{u}^{n+1} + \frac{1}{\rho_0}\frac{\partial \hat{p}^{n+1}}{\partial x} = -\hat{v}^{n+1}\frac{\partial u_0}{\partial y} \tag{40}$$

$$\hat{v}^{n+1} + \frac{\hat{p}^{n+1}}{Z} = 0 \tag{41}$$

$$-i\omega\frac{\hat{p}^{n+1}}{Z} + \frac{1}{\rho_0}\frac{\partial \hat{p}^{n+1}}{\partial y} = 0 \tag{42}$$

After the discretization of these equations, the ghost point values are found conveniently from the interior solutions and then $\hat{u}^{n+1}$, $\hat{v}^{n+1}$ and $\hat{p}^{n+1}$ are obtained at the soft wall by using the interpolation formula given by Eq.(34) at every current iteration level n+1.

The gradient of the acoustic pressure normal to the wall is set to zero on a hard wall

$$\frac{\partial \hat{p}^{n+1}}{\partial y} = 0 \tag{43}$$

This condition is discretized as wall derivative in Appendix A. Ghost point values are found from the interior solutions and then $\hat{p}^{n+1}$ is obtained at the hard wall using the interpolation formulas given by Eqs.(34) and (35) at every current iteration level n+1.

It has been found that the outlet boundary conditions hinder the convergence of the solution. To improve convergence, the complex form of the characteristic c_4 (Eq.(17)) is set to zero, and other characteristics are obtained by second order extrapolation from the interior solutions. Extrapolation is given as

$$q_{i,j} = 2\,q_{i-1,j} - q_{i-2,j} \tag{44}$$

where q is any variable (c_2, c_3, c_4). The primitive solutions $\hat{u}^{n+1}$, $\hat{v}^{n+1}$ and $\hat{p}^{n+1}$ are obtained from

$$\hat{u}^{n+1} = 0.5\,(c_3 + c_4)/\rho_0 c_0 \tag{45}$$

$$\hat{v}^{n+1} = c_2/\rho_0 c_0 \tag{46}$$

$$\hat{p}^{n+1} = 0.5\,(c_3 + c_4) \tag{47}$$

where c_2, c_3, c_4 are in complex form.

3.3 Artificial Dissipation

Truncated terms in finite difference equations indicate the accuracy; that is, these terms are not taken into consideration in the solution method. If we modify a finite difference equation after some algebraic manipulation by applying Taylor series expansion, we find the dominant error term of the finite difference equation. The coefficient of the dominant even order term in the error is known as artificial viscosity [23,24]. This is a nonphysical coefficient introduced by a particular approximation of the partial differential equation. The error term results in an inaccurate solution, revealing themselves as numerical oscillations. However, it is not a practical application in numerical computations. Therefore, an artificial dissipation term is added explicitly to the scheme to control nonphysical numerical oscillations, and at the same time to improve the stability of the scheme.

Fourth-order artificial dissipation with a constant coefficient [11] is used. It is given as

$$D(\mathbf{Q}) = -\frac{k}{\Delta t}(\delta_x + \delta_y)\mathbf{Q} \tag{48}$$

where Δt is the time increment, constant coefficient k is 1/128, and fourth-order operators in the x- and y-directions are

$$\delta_x Q_{i,j} = Q_{i-2,j} - 4Q_{i-1,j} + 6Q_{i,j} - 4Q_{i+1,j} + Q_{i+2,j} \quad (49)$$

$$\delta_y Q_{i,j} = Q_{i,j-2} - 4Q_{i,j-1} + 6Q_{i,j} - 4Q_{i,j+1} + Q_{i,j+2} \quad (50)$$

3.4 Stability Analysis

Although a finite difference approximation to a partial differential equation may be consistent, the solution will not necessarily converge. In the solution of finite difference equations, the computed solution is affected by round–off errors and discretization errors. Round-off errors are a property of the computer, or by the application of a particular numerical method. In some cases, the magnitude of the round-off error is proportional to the number of grid points in the computational domain; refining the grid decreases truncation error but increases round-off error. If the errors introduced into the finite difference equations are not controlled, the growth of errors with the solution of the finite difference equations will result in an unstable solution. Therefore, it is essential to understand and control these errors by stability analysis for a successful solution. In other words, it is essential to determine stability requirements of finite difference equations. One of the methods for stability analysis is the Von Neumann stability analysis [23].

Von Neumann stability analysis is applied to linear equations, and the effect of the boundary conditions on the stability of the solution is not included. In this method, a solution of the finite difference equations is expanded into a Fourier series. It is sufficient to investigate only one component of the Fourier series. This component is substituted into discretized equations and then an amplification factor (or amplification matrix) is found. Amplification factor (or the largest eigenvalue of the amplification matrix for a system of equations) indicates whether or not the

numerical algorithm is stable. Extension of stability region is more important than the order of accuracy for a numerical algorithm. Our mathematical model given in Chapter 2 is categorized as a 2D system of equations.

We start with assuming a Fourier component of the form

$$\boldsymbol{q}_{i,j}^{n} = \boldsymbol{Q}^{n}\, e^{I k_x (\Delta x) i}\, e^{I k_y (\Delta y) j} \tag{51}$$

Similarly,

$$\boldsymbol{q}_{i\pm 1,j}^{n} = \boldsymbol{Q}^{n}\, e^{I k_x (\Delta x)(i\pm 1)}\, e^{I k_y (\Delta y) j} \tag{52}$$

$$\boldsymbol{q}_{i,j\pm 1}^{n} = \boldsymbol{Q}^{n}\, e^{I k_x (\Delta x) i}\, e^{I k_y (\Delta y)(j\pm 1)} \tag{53}$$

where $\boldsymbol{q}$ is the vector of the dependent variables $(\hat{u}, \hat{v}, \hat{p})$, $\boldsymbol{Q}^n$ is the amplitude at time level n, k_x and k_y are the wave numbers in the x- and y-directions, $I = \sqrt{-1}$, i and j represent components, $k_x \Delta x$ and $k_y \Delta y$ are phase angles.

The set of pseudo time-marching-modeled equations with artificial dissipation is expressed as a vector equation, and it is given by

$$\frac{\partial \boldsymbol{q}}{\partial t} + [A]\boldsymbol{q} + [B]\frac{\partial \boldsymbol{q}}{\partial x} + [C]\frac{\partial \boldsymbol{q}}{\partial y} + [S]\boldsymbol{q} - [D]\boldsymbol{q} = 0 \tag{54}$$

where $[A]$, $[B]$, and $[C]$ are the coefficient matrices, $[S]$ is the coefficient matrix of the source vector $s(\boldsymbol{q})$, $[D]$ is the coefficient operator matrix of artificial dissipation. Discretizing the equations, substituting the Fourier components defined in Eqs.(51), (52), and (53) canceling common terms and factoring $\boldsymbol{Q}^n$, and applying the four-stage compact Runge-Kutta scheme, we obtain

$$\boldsymbol{Q}^{n+1} = \left\{ [ID] - \sum_{p=1}^{4} \frac{(-1)^p}{p!} (\Delta t)^p \left([R]^p - [R]^{p-1}[D] \right) \right\} \boldsymbol{Q}^{n} \tag{55}$$

where $[ID]$ is the identity matrix, $[R]$ is the operator matrix of residuals, and $[D]$ is the operator matrix of artificial dissipation. These operators are given by

$$[R] = [A] + [B]\ \delta_{Fx} + [C]\ \delta_{Fy} + [S] \tag{56}$$

$$[D] = [ID]\frac{(-k)}{\Delta t}(\delta_{Dx} + \delta_{Dy}) \tag{57}$$

Here, Fourier transform of finite difference operators are represented as

$$\frac{\partial}{\partial x} \Rightarrow \delta_{Fx}\ ,\quad \frac{\partial}{\partial y} \Rightarrow \delta_{Fy} \tag{58}$$

and Fourier transform of artificial dissipation operators in both x- and y-directions are represented as

$$\partial_{Dx} \Rightarrow \delta_{Dx}\quad ,\quad \partial_{Dy} \Rightarrow \delta_{Dy} \tag{59}$$

The amplification matrix is obtained from Eq.(56)

$$[G] = [ID] - \sum_{p=1}^{4} \frac{(-1)^p}{p!}(\Delta t)^p \left([R]^p - [R]^{p-1}[D]\right) \tag{60}$$

where $[G]$ is amplification matrix. Stability requires that the largest eigenvalue of the amplification matrix be less than or equal one. The mathematical requirement is that, if eigenvalue λ is real, then $|\lambda_{G\max}| \le 1$, and if eigenvalue λ is complex, then $|\lambda_{G\max}|^2 \le 1$.

For fourth-order accurate central differencing in space, the operator δ_{Fx} in the x-direction is

$$\begin{aligned}\delta_{Fx} &= (e^{-2I k_x\Delta x} - 8e^{-I k_x\Delta x} + 8\ e^{-I k_x\Delta x} - e^{2I k_x\Delta x}) / (12\ \Delta x) \\ &= (\ 16I\sin(k_x\Delta x) - 2I\sin(2\ k_x\Delta x)\ ) / (12\ \Delta x)\end{aligned} \tag{61}$$

and for fourth-order artificial dissipation, the operator δ_{Dx} in the x-direction is

$$\begin{aligned}\delta_{Dx} &= e^{-2I k_x\Delta x} - 4e^{-I k_x\Delta x} + 6 - 4e^{-I k_x\Delta x} + e^{2I k_x\Delta x} \\ &= 6 - 8\cos(k_x\Delta x) + 2\cos(2\ k_x\Delta x)\end{aligned} \tag{62}$$

A code has been written in Matlab because of the simplicity provided for matrix operations, but it should be noted that this algorithm with RK4 scheme is very sensitive to numerical errors. In Matlab, $\sin(\pi)$ and $\cos(\pi/2)$ are not exactly zero, because pi (π) is not exactly equal π. Therefore, we intentionally set them to zero, thus, acceptable results, $\lambda \leq 1$, are obtained. Because of symmetry, dimensionless frequency space covered by the phase angles, $k_x\Delta x$ and $k_y\Delta y$, are chosen as $(0, \pi)$.

Figure 3.2 shows the maximum eigenvalue of the amplification matrix of the scheme for the governing equations with various $k_y\Delta y$. These results are approximately same for all peak Mach numbers (0.1-0.3) and all frequencies (500-3000 Hz). It should be noted that in a region up to $k_x\Delta x = \pi/6$ and up to $k_y\Delta y = \pi/6$ waves are not damped properly because eigenvalues are slightly greater than one, such as 1.0001, but, the scheme did not create significant problems.

The maximum eigenvalue of amplification matrix of the scheme for hard-wall conditions with various $k_y\Delta y$ is shown in Fig. 3.3. These results are approximately the same for all peak Mach numbers (0.1-0.3) and all frequencies (500-3000Hz). It is clear from this figure that $|\lambda_{G\max}|^2$ is constant at unity. This indicates that scheme is neutrally stable.

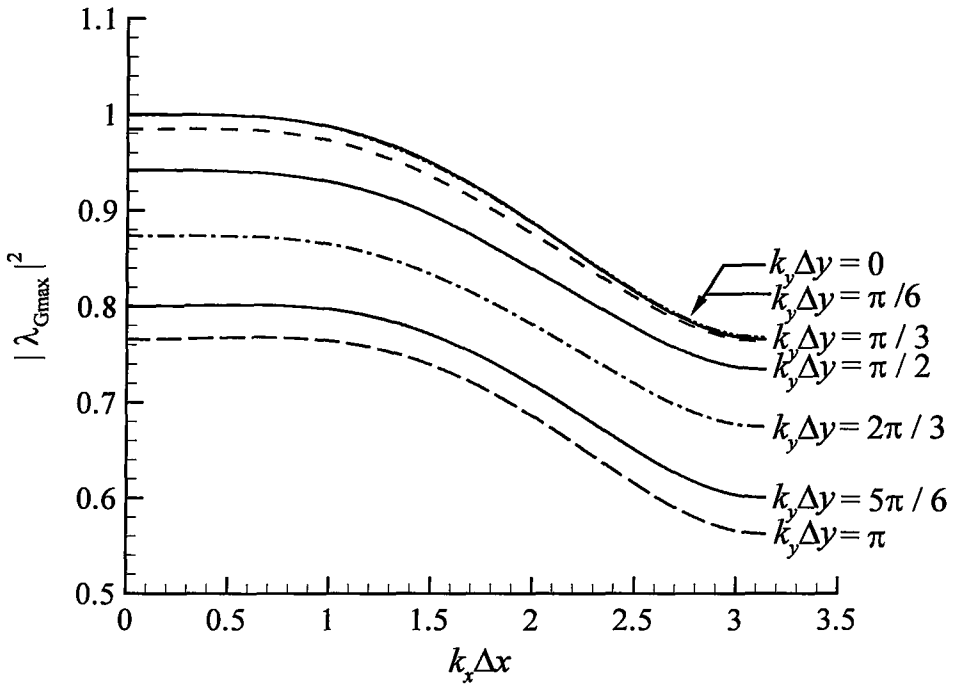

Figure 3.2 Maximum eigenvalue of amplification matrix of the scheme for governing equations with various $k_y\Delta y$.

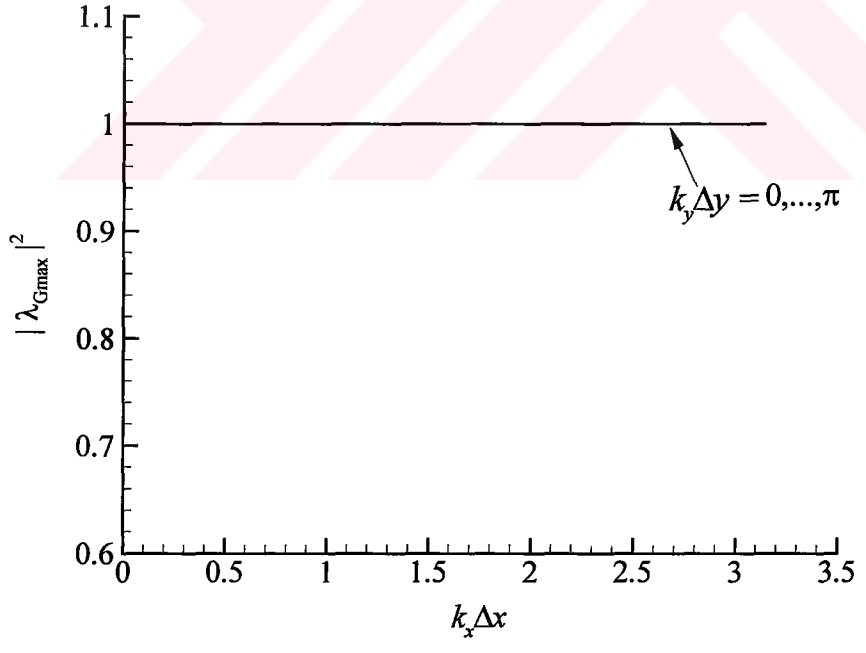

Figure 3.3 Maximum eigenvalue of amplification matrix of the scheme for hard-wall conditions with various $k_y\Delta y$.

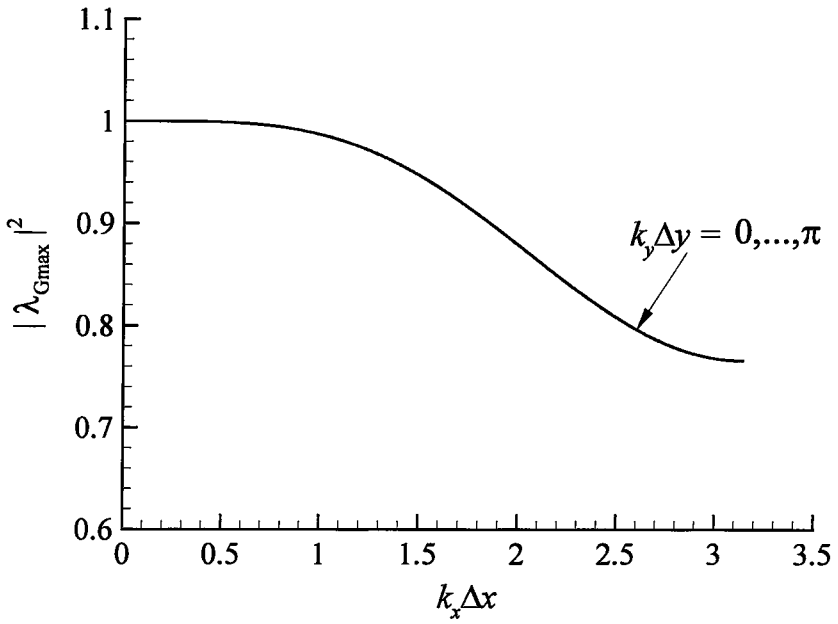

Figure 3.4 Maximum eigenvalue of amplification matrix of the scheme for soft-wall conditions with various $k_y\Delta y$.

Figure 3.4 shows the maximum eigenvalue of amplification matrix of the scheme for soft-wall conditions with various $k_y\Delta y$. These results are approximately the same for all peak Mach numbers (0.1-0.3) and all frequencies (500-3000 Hz). Acoustic waves are not damped properly in a region up to $k_x\Delta x = \pi/3$ and up to $k_y\Delta y = \pi/3$ because eigenvalues are slightly greater than one, such as 1.0002, but, as pointed out above the scheme did not create significant problems.

Stability analysis of this algorithm shows that in some regions, the eigenvalues of amplification matrix become equal to one, signifying a neutrally stable algorithm. Therefore, it is expected that this numerical algorithm may become unstable. To increase the stability and for an effective convergence we implicitly modify the hard-wall, soft-wall, and outlet quantities by using inside values at every iteration level. In other words, after every R-K iteration, wall conditions are applied explicitly, using the available interior solution.

CHAPTER 4

RESULTS AND DISCUSSION

Frequency-domain simulations of the NASA Langley flow-impedance tube are performed at the same conditions as the time-domain simulations of reference [16]. Two-dimensional schematic of the test section of the flow impedance tube is shown in Fig. 1.7. The background flow is sheared and the mean flow velocity profile is given by

$$u_0(y) = 4 M_{pk} c_0 \left(\frac{y}{h}\right)\left(1 - \frac{y}{h}\right) \tag{63}$$

where h is the duct height and M_{pk} is mean-flow centerline Mach number. The mean flow velocity depends only on y. It is clear that at the hard wall boundaries, $y = 0$ and $y = h$, the mean flow velocity is equal to zero. This assumption resembles a fully developed laminar flow in a duct and supplies close conditions to the actual flow.

Numerical simulations are performed and compared with time-domain results and experimental data at the aforementioned conditions. At the inlet boundary, there is a source that generates plane acoustic waves at desired frequencies and sound pressure levels (SPLs). Acoustic waves are chosen at frequencies from 0.5kHz to 3.0 kHz with 0.5 kHz increments and with SPL of 130 dB for each frequency. Mean-flow centerline Mach numbers M_{pk} are chosen as 0.1, 0.3, and 0.5. Simulations are

performed with different resolutions for different Mach numbers to obtain adequate results. An important parameter used to determine the mesh size is the number of grid points per wavelength (NPPW) in the x- and y-directions. The computations are carried out on meshes with a resolution of $\text{NPPW}_x = 23$ for the highest frequency (3.0 kHz). In general, meshes of 188x14, 252x14, 344x14 grid points are used at Mach numbers 0.1, 0.3, and 0.5, respectively, for all frequencies.

A constant depth ceramic tubular liner is used as the acoustic treatment panel. The same impedance data as those used in the time-domain simulations are used. Although the impedance of the liner is influenced by the adjacent sound field and flow field, at all Mach numbers the same impedance data are used, because grazing flow effects on the impedance of the material used were relatively insignificant [19].

As it was pointed out earlier, acoustic treatment panel causes generation of additional modes that propagate in both upstream and downstream directions. Experiment and time-domain simulations [16] showed that these propagating modes are not sufficiently attenuated; thus, SPLs are slightly different from SPLs of incoming waves at the inlet section. Therefore, results are fitted to experimental SPLs at source plane to be able to compare with the time-domain results and experimental data.

4.1 Effects of Grid Resolution and Boundary Conditions

4.1.1 Effects of Grid Resolution

Grid resolution is an important parameter to obtain adequate results, and also important for computational cost. In our study, we performed the simulations with

the lowest mesh resolution of 23 cells per wavelength for the highest frequency (3.0 kHz) at all Mach numbers. It is useful to test whether or not the simulations with a finer mesh resolution will give better results. Moreover, as will be seen from figures, we encountered extremely small reflections in SPL (maximum 2 dB) at the outlet boundary. To retain accuracy, more grid points per wavelengths may be needed.

For these reasons, we increased the grid resolution in the x-direction for the same computational domain (standard domain) and performed the simulations for frequencies of 0.5, 1.0, and 3.0 kHz at all Mach numbers. Comparisons are illustrated in Figs. 4.1, 4.2, and 4.3 for Mach numbers 0.1, 0.3, and 0.5, respectively, in which the solid lines indicate the results for the standard domain and the dashed-dotted lines indicate the results for a finer mesh ($NPPW_x = 29$ and $NPPW_x = 32$).

4.1.1.1 $M_{pk} = 0.1$ Case

In Figure 4.1 the standard domain results are compared with a finer mesh for frequencies of 0.5, 1.0, and 3.0 kHz. At this Mach number simulations for the standard domain were performed on a mesh with 23 cells per wavelength (188x14 grid), and simulations for the standard domain with a finer mesh were performed on a mesh with 29 cells per wavelength (220x14 grid) for the highest frequency (3.0 kHz). As shown in figure, the results for the two mesh resolutions appear to be almost identical. This means that the results are grid independent at this Mach number.

As clear from the figures that the liner causes attenuation of the sound waves. This depends on the sound frequency content of the waves. The liner we used was

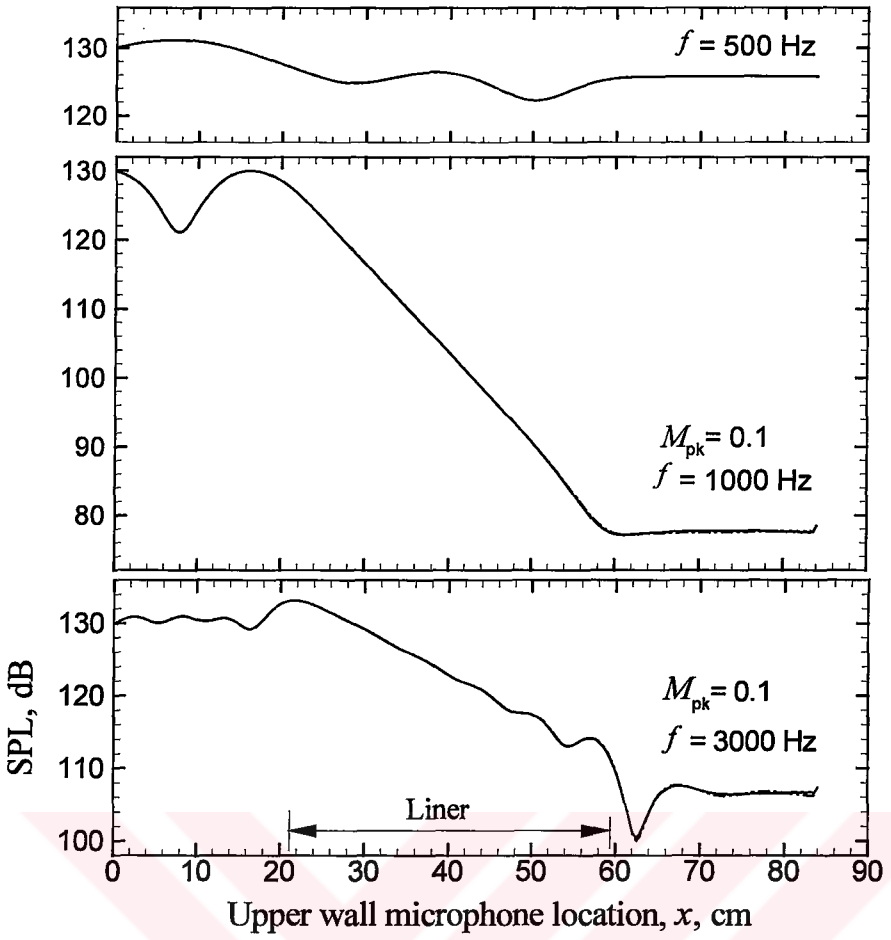

Figure 4.1 Effects of grid resolution on the solution for frequencies of 0.5, 1.0, and 3.0 kHz at $M_{pk} = 0.1$: ——, $NPPW_x = 23$ at 3.0 kHz;----- , $NPPW_x = 29$ at 3.0 kHz.

tuned to be more effective at 1.0 kHz. Therefore, the results indicate more attenuation at this particular frequency. The oscillatory nature of the SPL curves near the liner leading edge and trailing edge are because of the additional modes generated by the liner itself. These modes combine with or cancel the incident waves as they propagate.

4.1.1.2 $M_{pk} = 0.3$ Case

Figure 4.2 displays and compares the results with a finer mesh results for frequencies of 1.0 and 3.0 kHz. For the standard domain simulations, a mesh

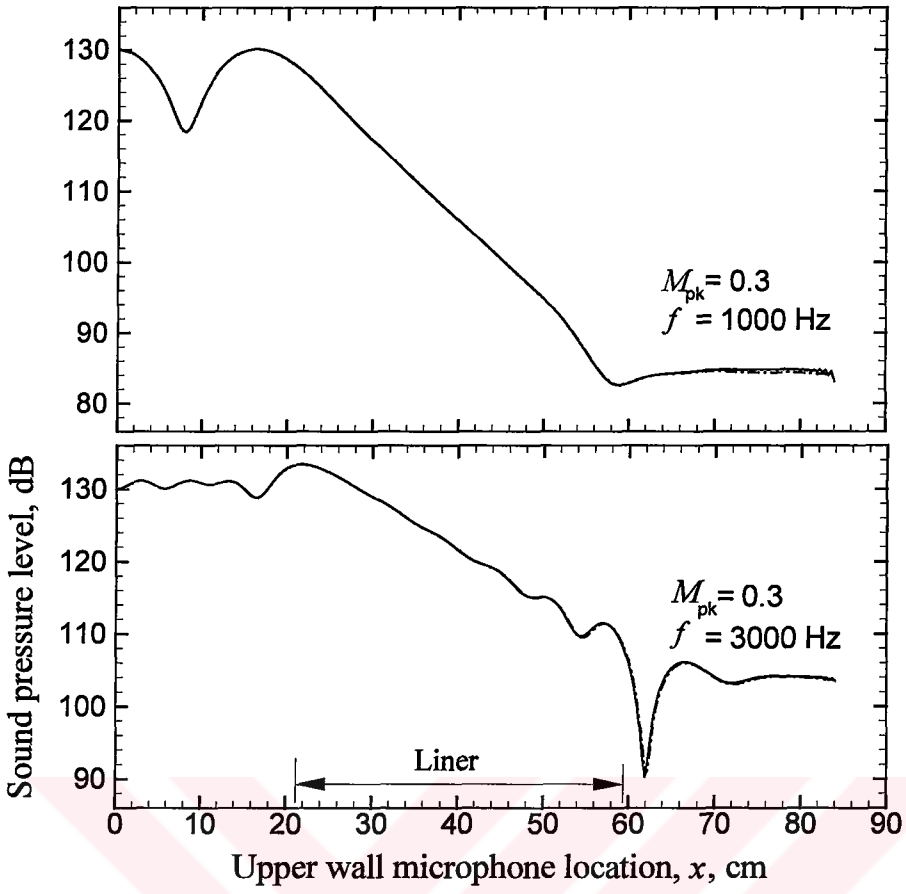

Figure 4.2 Effects of grid resolution on the solution for frequencies of 1.0 and 3.0 kHz at $M_{pk} = 0.3$: ——, $NPPW_x = 23$ at 3.0 kHz; -----, $NPPW_x = 32$ at 3.0 kHz.

resolution of $\lambda_x/\Delta x = 23$ was used, and for simulations on the standard domain with a finer mesh, a mesh resolution of $\lambda_x/\Delta x = 32$ was used for the highest frequency. As shown in the figure, the differences between the results are insignificant. For both grid resolutions, extremely small reflections in SPL are seen at the outlet boundary. This indicates that the solutions are not affected by the grid resolution at this Mach number.

Since we encountered numerical instabilities at the f = 0.5 kHz case, no comparison is presented at this frequency. As mentioned in section 3.4 the stability requirement was that the largest eigenvalue of the amplification matrix be less than

or equal one. At some phase angles, the maximum eigenvalues were slightly out of the stability region in the present numerical method for the impedance and inflow conditions. These small differences appeared to have significant effects on the solution for 0.5 kHz at M_{pk} = 0.3, as will also be for 0.5 and 1.0 kHz at M_{pk} = 0.5. Therefore, the simulation on a 252x14 mesh failed at 0.5 kHz. For this reason, we reduced the grid resolution for this frequency and performed a simulation with a grid resolution of 106 cells per wavelength (188x14). This resolution was more than sufficient for the solution. It should be noted that the maximum allowable grid resolution for this case was determined as $\lambda_x / \Delta x$ = 124 (220x14 grid). When the mesh resolutions were chosen greater than this the simulations failed.

4.1.1.3 M_{pk} = 0.5 Case

The results for the standard domain with a finer mesh are compared for the frequency of 3.0 kHz. The results are shown in Figure 4.3. For this case the standard domain mesh resolution is $\lambda_x / \Delta x$ = 23 and finer mesh resolution is $\lambda_x / \Delta x$ = 34. Although small reflections are seen for both grid resolutions at the outlet boundary, the agreement between the simulations is very good. The differences between the results are insignificant.

The results for the 0.5 and 1.0 kHz cases are not presented, because the simulations failed for the same reason as explained at M_{pk} = 0.3 case. At this Mach number, standard domain simulations were performed on a 344x14 mesh. At 0.5 kHz, simulation could not be performed for any grid resolution, but reducing the grid resolution we were able to attain a solution for 1.0 kHz. We determined the

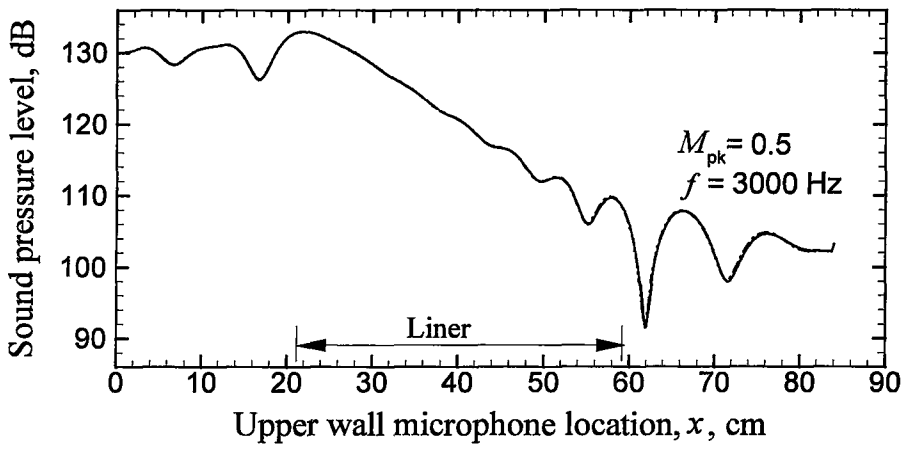

Figure 4.3 Effects of grid resolution on the solution for frequency of 3.0 kHz at $M_{pk} = 0.5$: ——, $NPPW_x = 23$; - - - - - , $NPPW_x = 32$.

maximum allowable grid resolution for 1.0 kHz as $\lambda_x / \Delta x = 44$ (220x14 grid) for stability reasons. These results indicate that numerical instabilities are very effective for low frequencies, which can be seen in the stability analysis section in Chapter 3. However, for higher frequencies, as shown in the figure, the results are not affected by increasing the grid resolution when the stability conditions are met.

4.1.2 Boundary Condition Effects

As indicated previously, the inlet and outlet boundaries of the domain are free artificial boundaries, and nonreflecting boundary conditions are used at these sections. An advantage of these conditions is that calculations can be performed on a much smaller computational domain. Therefore, it is needed to test whether or not these conditions work accurately for the cases of our interest. For this, computational domain is extended to downstream (from x = 0 cm to 126.6 cm) and sound pressure levels along the upper wall are compared for the frequencies of 0.5, 1.0, and 3.0 kHz at all Mach numbers. One-and-a half times more grid points in the

x-direction were used for the extended domain simulations, corresponding to a mesh of 23 cells per wavelength for the highest frequency (3.0 kHz), the same as that for the standard domain simulations. The results with the extended computational domain at Mach numbers 0.1, 0.3, and 0.5 are illustrated in Figs. 4.4, 4.5, and 4.6, respectively, in which the solid lines indicate the results for the standard domain (0-84cm) and the dashed-dotted lines for the extended domain to downstream (0-126.6cm).

4.1.2.1 $M_{pk} = 0.1$ Case

For this case the standard domain simulations were performed on a 188x14 mesh at all frequencies, and for the extended domain simulations, a 282x14 mesh was used with a grid resolution of $\lambda_x / \Delta x = 23$ for the highest frequency ($f = 3.0$ kHz). The results are shown in Fig. 4.4. The comparisons of the results between the two domains reveal excellent agreement, indicating that the outlet boundary conditions work well at this Mach number.

4.1.2.2 $M_{pk} = 0.3$ Case

Due to the stability problem that we encountered at this Mach number, the standard domain simulations were performed on a 188x14 mesh for 0.5 kHz case and a 252x14 mesh for 1.0 and 3.0 kHz cases, still with sufficient resolution. For the extended domain simulations, a 282x14 mesh was used with a grid resolution of $\lambda_x/\Delta x = 106$ for 0.5 kHz case and a 378x14 mesh was used with grid resolutions of $\lambda_x / \Delta x = 71$ and $\lambda_x / \Delta x = 23$ for the 1.0 and 3.0 kHz cases, respectively.

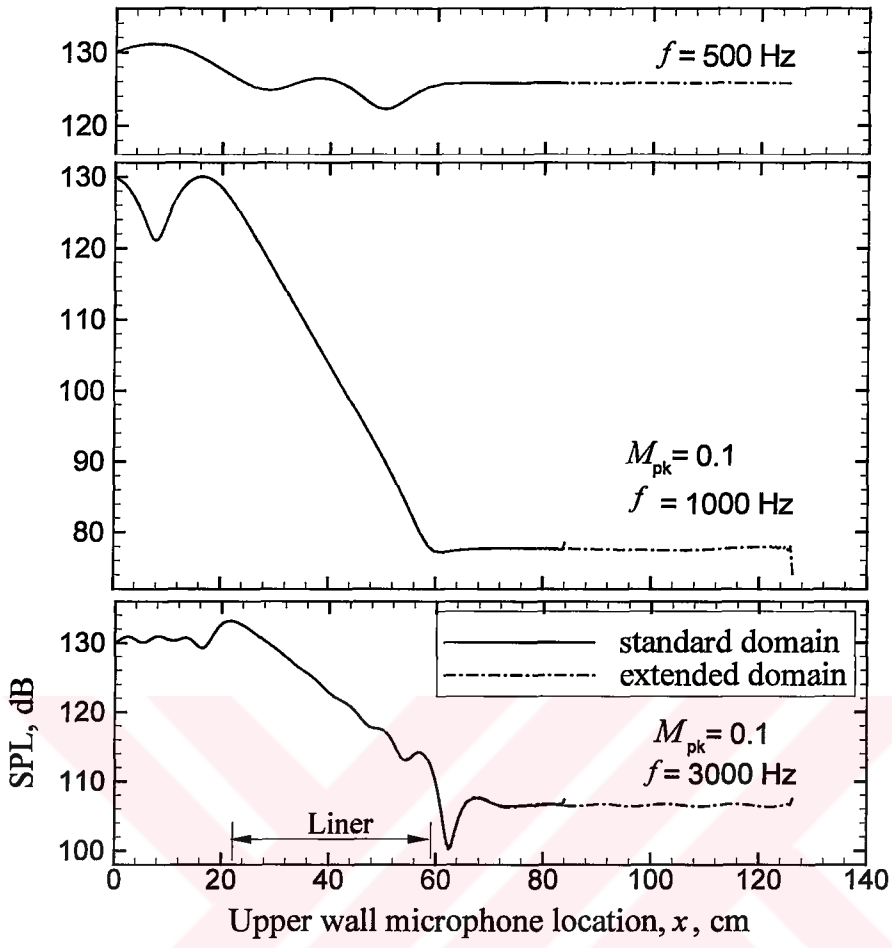

Figure 4.4 Sound pressure level along the upper wall using the standard domain and extended domain to downstream for frequencies of 0.5, 1.0, and 3.0 kHz at $M_{pk} = 0.1$.

Figure 4.5 shows and compares the results between the two domains. The same kind of trends are observed between the results for all cases. Insignificant reflections are again seen at the outlet sections of both domains at 1.0 and 3.0 kHz.

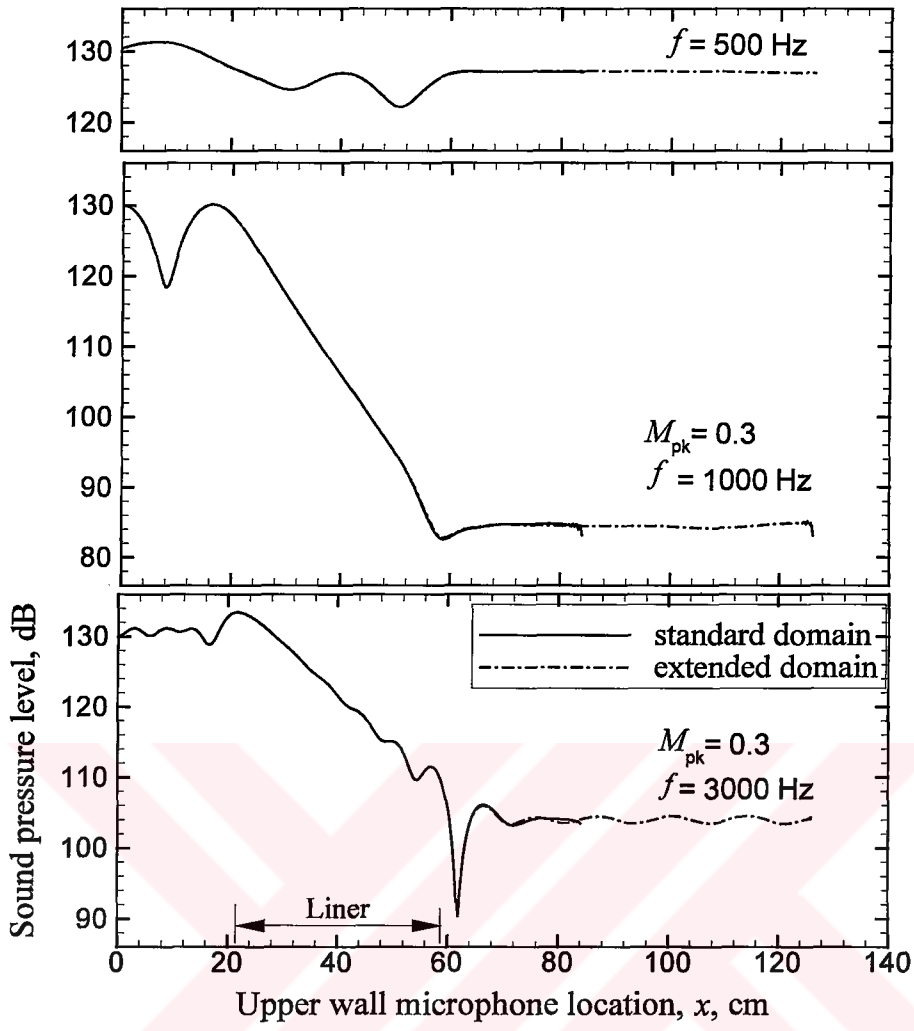

Figure 4.5 Sound pressure level along the upper wall using the standard domain and extended domain to downstream for frequencies of 0.5, 1.0, and 3.0 kHz at $M_{pk} = 0.3$.

4.1.2.3 $M_{pk} = 0.5$ Case

Comparison of the two domains for 0.1 and 0.3 kHz at Mach 0.5 is shown in Fig. 4.6. For $f = 0.5$ kHz, numerical simulations failed since numerical instabilities were more violent at this Mach number. The standard domain simulations were performed on a 188x14 mesh for the 1.0 kHz case and a 344x14 mesh for the

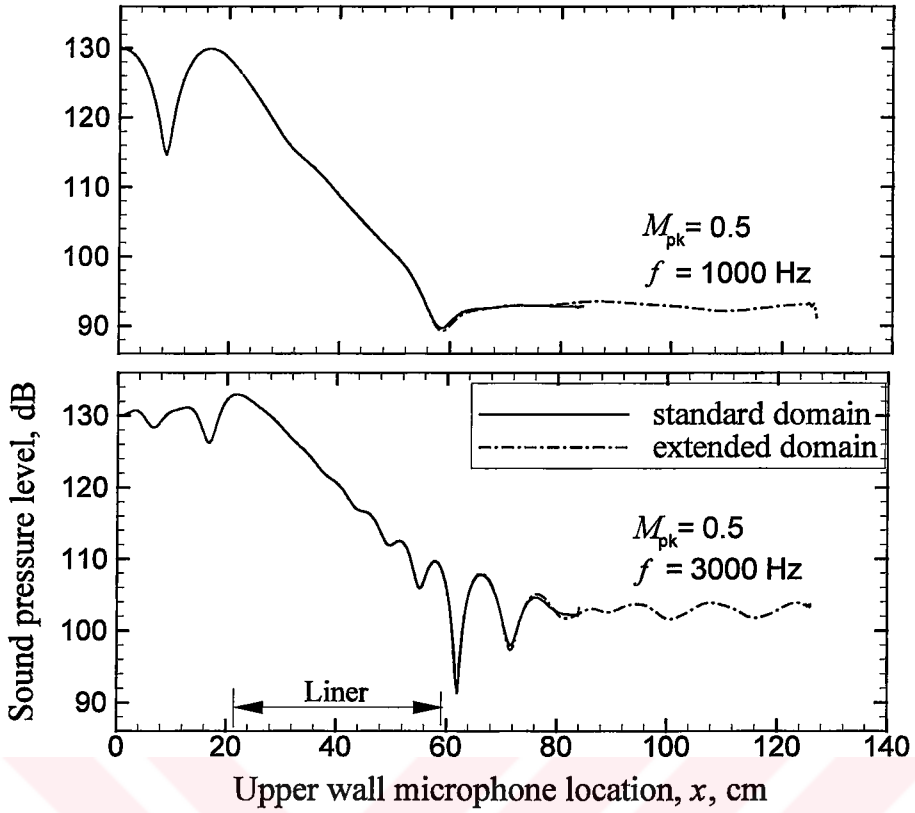

Figure 4.6 Sound pressure level along the upper wall using the standard domain and extended domain to downstream for frequencies of 1.0 and 3.0 kHz at $M_{pk} = 0.5$.

3.0 kHz case. For the extended domain simulations, a 282x14 mesh was used with a grid resolution of $\lambda_x / \Delta x = 37$ for the 1.0 kHz case and a 516x14 mesh was used with a grid resolution of $\lambda_x / \Delta x = 23$ for the 3.0 kHz case.

There are minor differences between the standard and extended domain solutions indicating the boundary conditions work accurately for this case, as well.

4.2 Comparisons with Time-Domain Simulations and Experiment

The impedance data we use in all simulations are the same as those used in the time-domain simulations, which approximated the impedance data using a curve fit

to the experiment. Therefore, our comparisons here should focus on the results of the present method and those of the time-domain method. Hence, some deviations from the experimental data are naturally expected at some frequencies because of the deviations from the experimental impedance which resulted from the functional fit of the impedance data [11]. The experimental impedance data and their approximations used in the time-domain simulations are given in Table 1. There are some small differences between the measured and fitted impedance values, especially for reactance, at some frequencies.

Table 1. Measured and fitted specific resistance and reactance values for the constant depth ceramic tubular liner (CT73).

Frequency KHz	$R/\rho_0 c_0$ (exp)	$R(\omega)/\rho_0 c_0$ (fit)	$X/\rho_0 c_0$ (exp)	$X(\omega)/\rho_0 c_0$ (fit)
0.5	0.41	0.40626	-1.56	-1.58720
1.0	0.46	0.47623	0.03	0.11325
1.5	1.08	1.07819	1.38	1.63812
2.0	4.99	5.00899	0.25	-0.27590
2.5	1.26	1.26291	-1.53	-1.23728
3.0	0.69	0.67333	-0.24	-0.28561

4.2.1 $M_{pk} = 0.1$ Case

The simulations for the $M_{pk} = 0.1$ case were performed on a 188x14 mesh with a mesh resolution of 23 cells per wavelength for the highest frequency (3.0 kHz). The frequency-domain results are compared with the time-domain results and experimental data using the standard domain (0-84 cm).

Figure 4.7 shows and compares the results for the case of $f = 0.5$ kHz. The solid line represents the frequency-domain result, the dashed-dotted-dotted line represents the time-domain result, and the symbols indicate the experimental data at

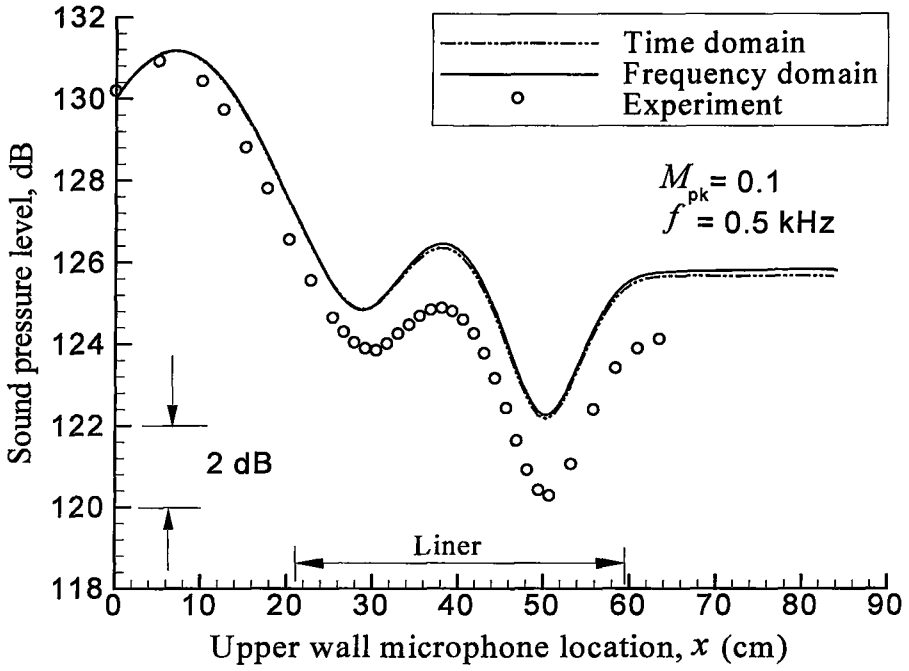

Figure 4.7 Sound pressure level along the upper wall given by frequency and time-domain simulations, and experiment at $f = 0.5$ kHz and $M_{pk} = 0.1$.

all figures in this subsection. It is evident that the differences between the frequency and time-domain simulations are small (about 0.2 dB). However, there appear to be some differences (maximum 2 dB) between the numerical results and experimental data. The reason for this could be the impedance data we used, which is extracted using some numerical techniques. Nonetheless, the numerical results and experimental data are in good agreement in general. As seen near the inlet region, the SPL tends to increase from 130 dB toward higher SPLs because of the upstream propagating waves. The reason for this is that the presence of the liner generates additional modes that propagate in both directions.

Comparison of the results for the case of $f = 1.0$ kHz is shown in Fig. 4.8. The details of the SPL curve were captured well and the frequency-domain results agree well with the time-domain results in general. But both of the simulations diverge to

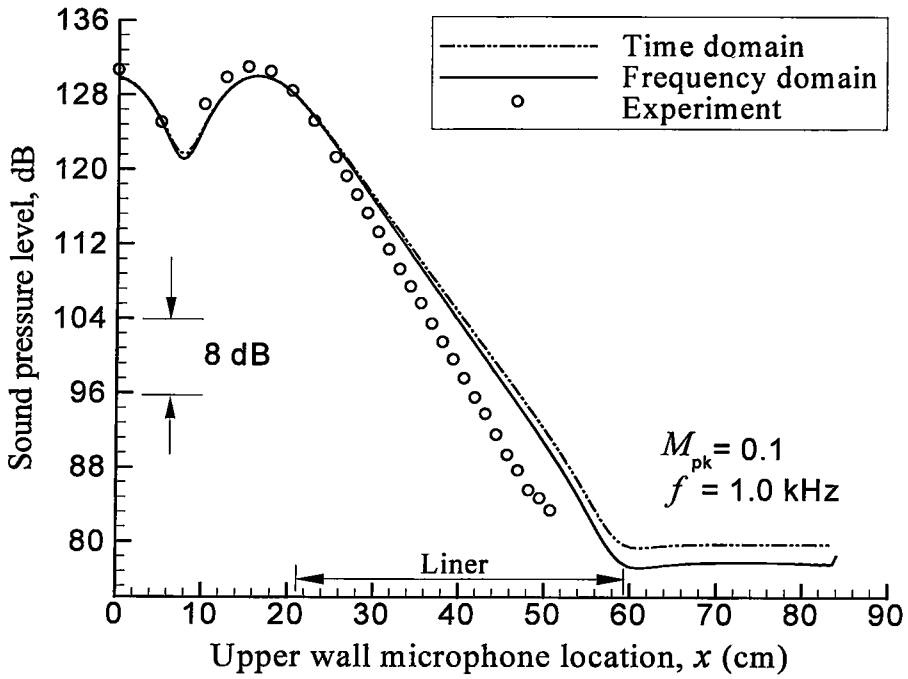

Figure 4.8 Sound pressure level along the upper wall given by frequency and time-domain simulations, and experiment at f = 1.0 kHz and M_{pk} = 0.1.

some small extent from the experimental data as the liner trailing-edge is approached. These differences are considered small because the change in the SPL between the inlet and outlet sections along the upper wall is about 52 dB, which indicates the pressure amplitude at the inlet section is actually 398 times greater than that in the outlet region and liner trailing-edge region.

In Figure 4.9, the results are compared for the case of f = 1.5 kHz. Again both the frequency-domain and time-domain methods captured the details of the SPL variation well, but they both have slightly different results than the experiment. Noting the total attenuation rate between the inlet and outlet sections, we may conclude that the liner is not very effective in suppression of the waves at 1.5 kHz. The differences between the experiment and the current results may be attributed to the approximations made to the background flow and experimental results. The

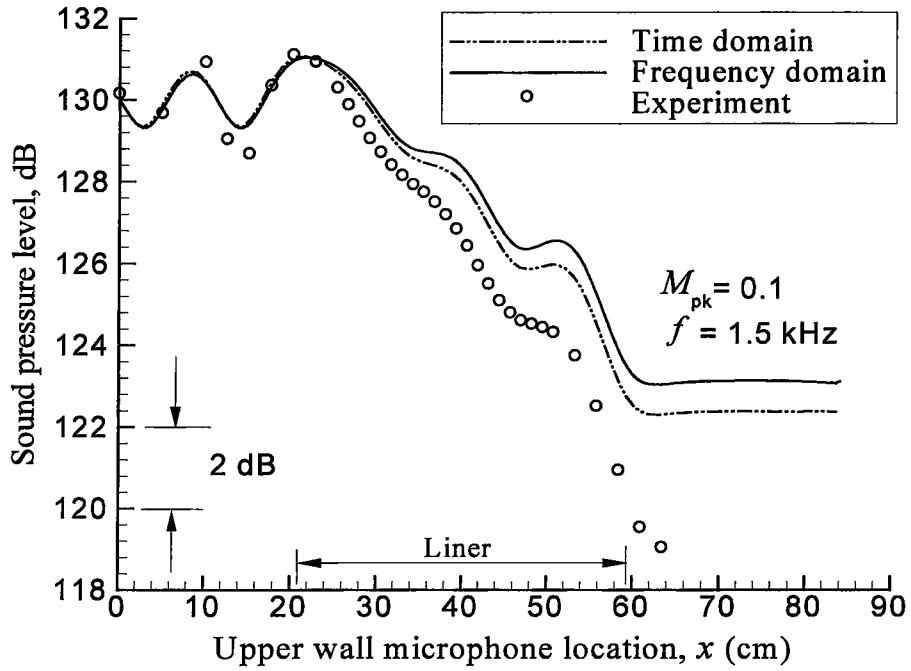

Figure 4.9 Sound pressure level along the upper wall given by frequency and time-domain simulations, and experiment at f = 1.5 kHz and M_{pk} = 0.1.

background flow was assumed fully developed. Use of a more realistic mean velocity profile could improve the results.

The simulations and experimental data are compared in Fig. 4.10 for the case of f = 2.0 kHz. The time-domain result agrees with experimental data better than the frequency-domain result. Although similar trends are observed in the results, frequency-domain result appears to deviate from the time-domain results and experimental data slightly.

Comparison of the results for the case of f = 2.5 kHz is shown in Fig. 4.11. The simulated SPLs (for frequency and time-domain) seem to agree well. Some deviation from the experimental data is observed as we approach to the liner trailing-edge region. This is mainly because of the slightly deviated resistance and reactance values we used as indicated before. Still the agreement between the simulated SPLs and experiment is good in general.

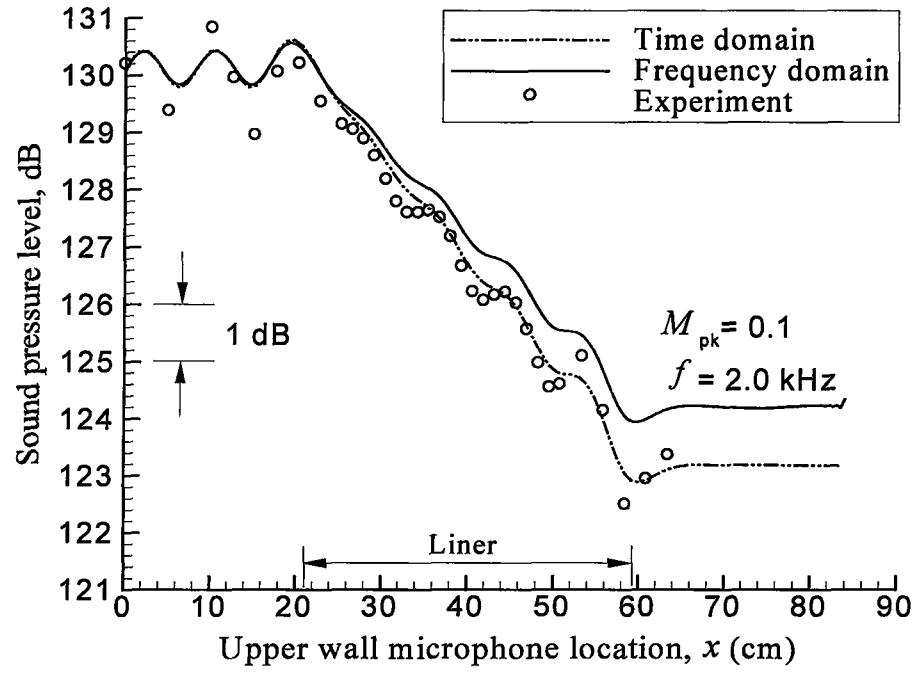

Figure 4.10 Sound pressure level along the upper wall given by frequency and time-domain simulations, and experiment at $f = 2.0$ kHz and $M_{pk} = 0.1$.

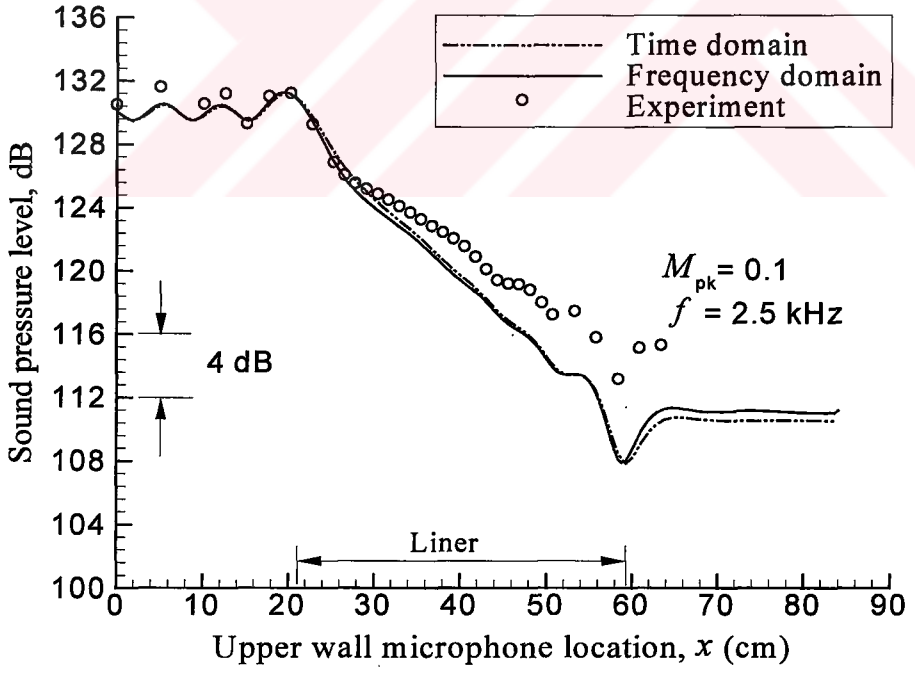

Figure 4.11 Sound pressure level along the upper wall given by frequency and time-domain simulations, and experiment at $f = 2.5$ kHz and $M_{pk} = 0.1$.

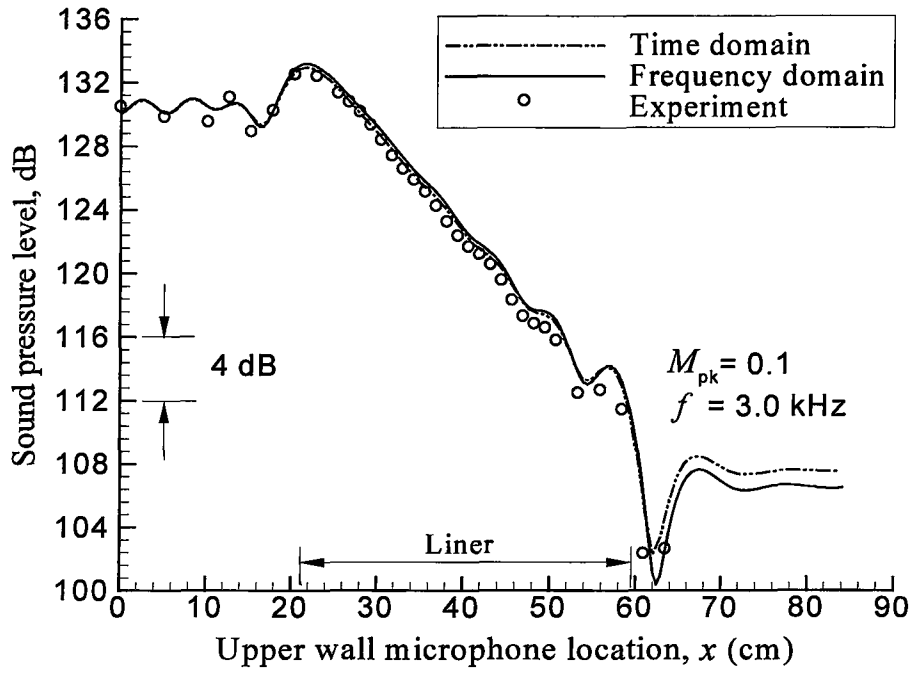

Figure 4.12 Sound pressure level along the upper wall given by frequency and time-domain simulations, and experiment at f = 3.0 kHz and M_{pk} = 0.1.

Figure 4.12 displays and compares the results for the case of f = 3.0 kHz. The trends for the calculated SPLs in the frequency-domain simulation follow very well those of the time-domain simulation and experiment. The effects of the impedance jumps are easily seen at liner leading and trailing-edge regions. At liner leading-edge region, the SPLs increase to the highest value (about 133 dB).

4.2.2 M_{pk} = 0.3 Case

For this case, a 188x14 mesh was used for the frequency of 0.5 kHz and a 252x14 mesh was used for the other frequencies with a grid resolution of 23 cells per wavelength for the highest frequency (3.0 kHz). Frequency-domain results are compared with time-domain results and experimental data using standard domain (0-84 cm). All results and experimental data indicate the sound pressure level (SPL) along the upper wall.

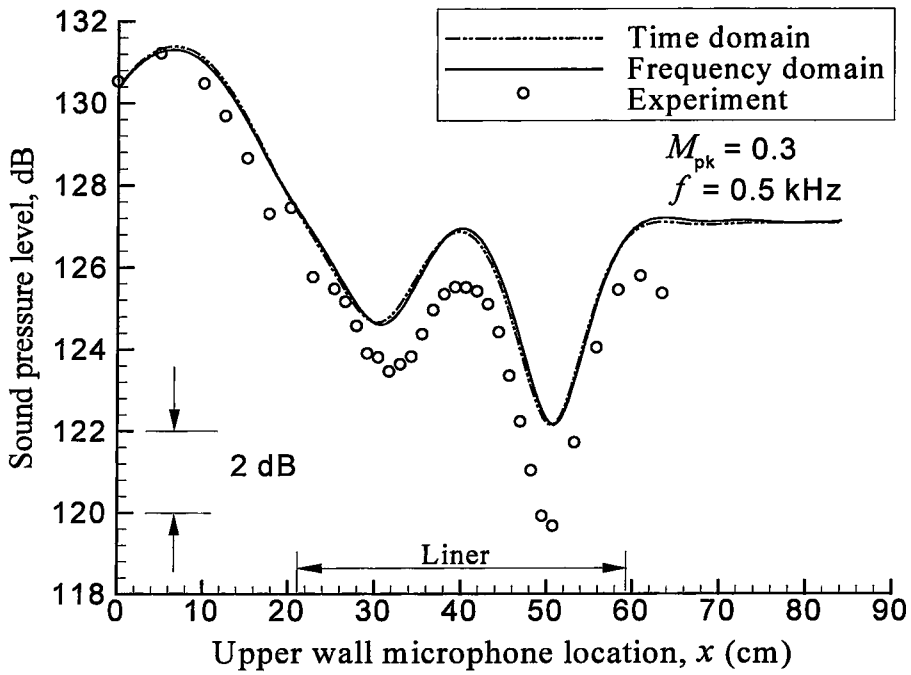

Figure 4.13 Sound pressure level along the upper wall given by frequency and time-domain simulations, and experiment at $f = 0.5$ kHz and $M_{pk} = 0.3$.

Figure 4.13 shows and compares the results for the case of $f = 0.5$ kHz. The solid line represents the frequency-domain result, the dashed-dotted-dotted line represents the time-domain result, and the symbol indicates the experimental data in all figures in this subsection. Since we encountered numerical instabilities at this frequency, the simulation with a 252x14 mesh failed. For this reason, the simulation was performed with a grid resolution of 106 cells per wavelength (188x14) for this frequency. In fact, this resolution was still more than sufficient for the solution.

The differences between the frequency- and time-domain simulations appear to be insignificant. The same kind of trends are observed between the numerical results and experimental data, The agreement between computations and experiment is also good in general.

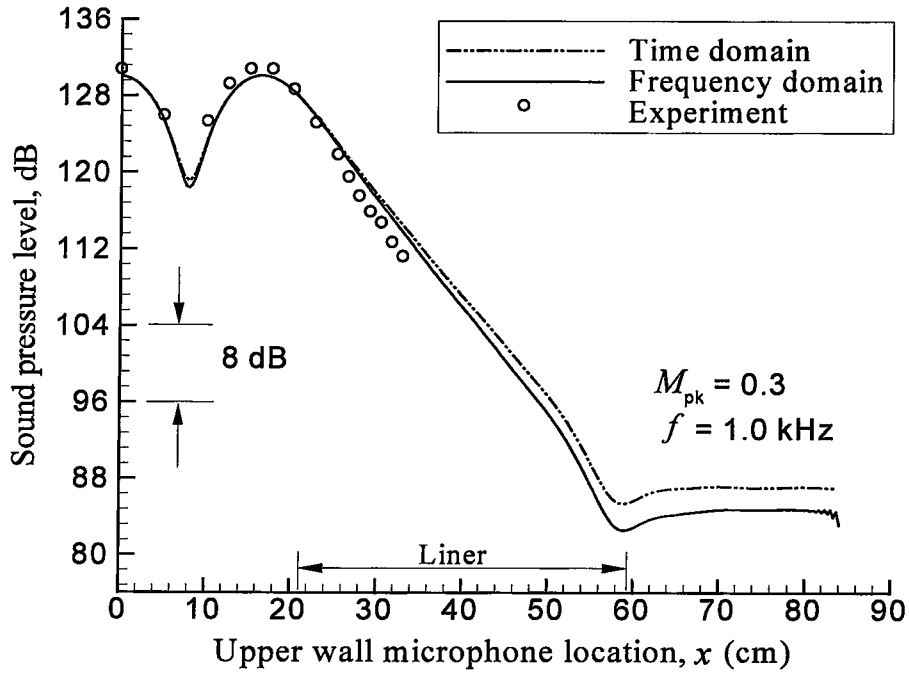

Figure 4.14 Sound pressure level along the upper wall given by frequency and time-domain simulations, and experiment at f = 1.0 kHz and M_{pk} = 0.3.

The results are compared for the case of f = 1.0 kHz in Fig. 4.14. No experimental data are shown after a certain microphone location. As noted in Özyörük et al. [11], the data fell below the background noise during the measurements at those on microphone locations. This is also valid for the frequencies of 3.0 kHz at M_{pk} = 0.3 and for the frequencies of 1.0 and 3.0 kHz at M_{pk} = 0.5. Although the frequency domain result appears to deviate from the time-domain result approaching the liner trailing-edge, the differences are small, and at the same time the frequency-domain result agrees with the experimental data better than the time-domain result.

In Figure 4.15, the results are compared for the case of f = 1.5. The numerical results appear to deviate from the experimental data near the liner trailing edge when the results are compared with the M_{pk} = 0.1. Similar trends are observed in the

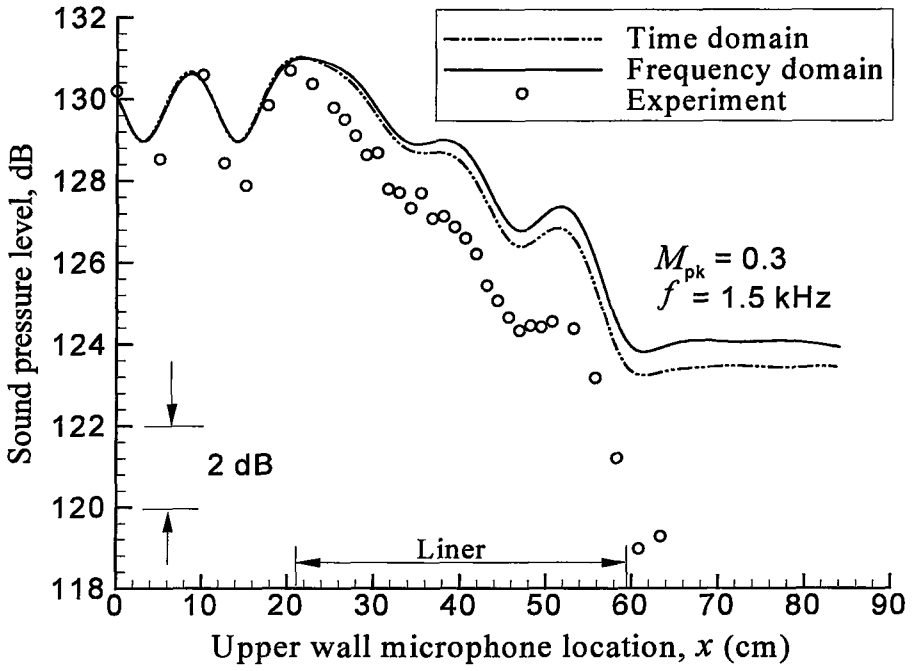

Figure 4.15 Sound pressure level along the upper wall given by frequency and time-domain simulations, and experiment at f = 1.5 kHz and M_{pk} = 0.3.

results, and the time-domain simulation agrees with the experiment better than the frequency-domain simulation.

Figure 4.16 displays and compares the results for the case of f = 2.0 kHz. An improvement is observed when the frequency-domain simulation is compared with the M_{pk}= 0.1. The frequency-domain result is in very good agreement with time-domain result and experimental data.

The simulations and experimental data are compared for the case of f = 2.5 kHz in Fig. 4.17. The trends for the calculated SPLs in frequency-domain simulation follow well those for the time-domain simulation and experiment. The simulated SPLs (for frequency and time domain) seem to be similar. A sudden rise toward to the highest SPL in the liner leading-edge region and a sudden fall toward the lowest SPL in the liner trailing-edge region are observed because of the generation of

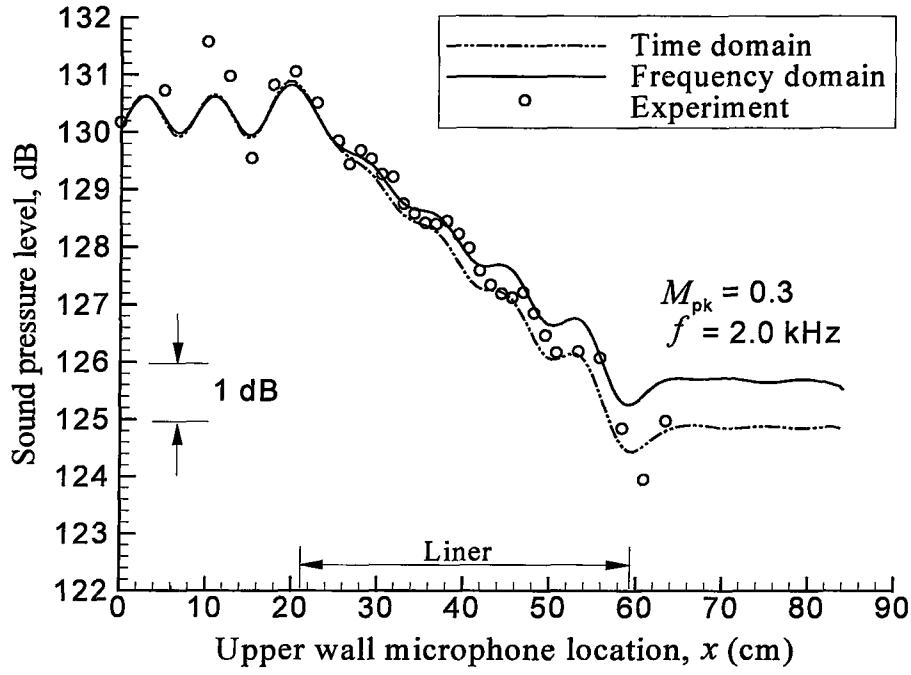

Figure 4.16 Sound pressure level along the upper wall given by frequency and time-domain simulations, and experiment at $f = 2.0$ kHz and $M_{pk} = 0.3$.

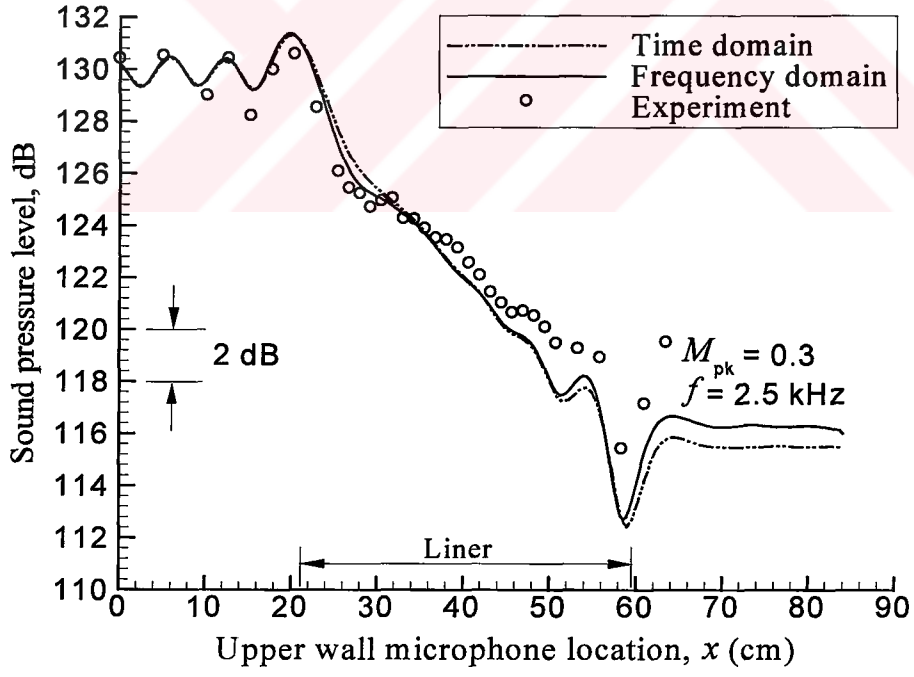

Figure 4.17 Sound pressure level along the upper wall given by frequency and time-domain simulations, and experiment at $f = 2.5$ kHz and $M_{pk} = 0.3$.

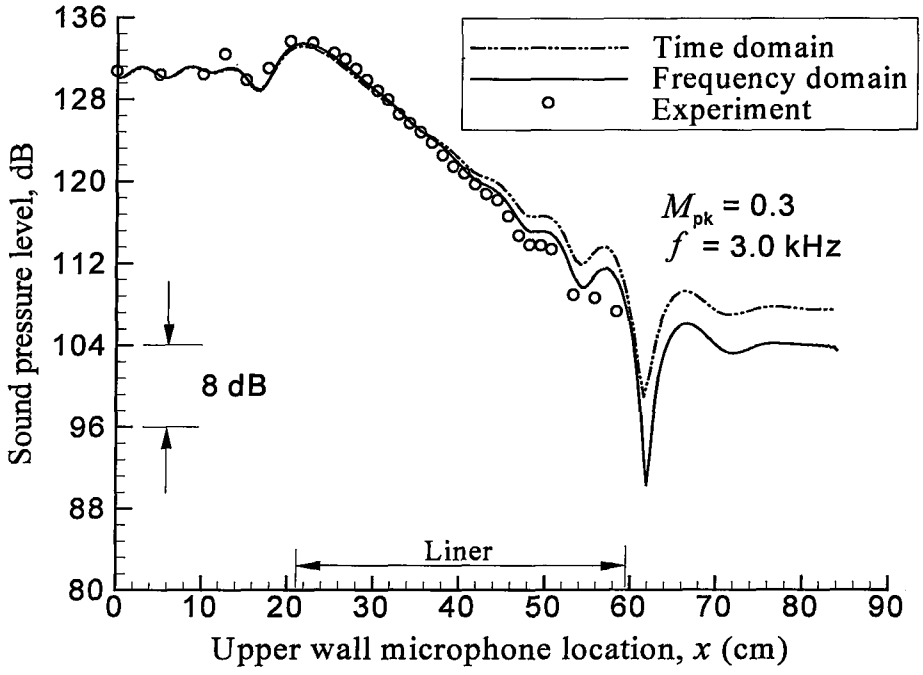

Figure 4.18 Sound pressure level along the upper wall given by frequency and time-domain simulations, and experiment at f = 3.0 kHz and M_{pk} = 0.3.

additional modes there. Wave reinforcements and cancellations become more pronounced in the liner leading- and trailing-edge regions at higher frequencies and Mach numbers.

Figure 4.18 shows and compares the results for the case of f = 3.0 kHz. The frequency-domain result agrees with the experimental data better than the time-domain result. When the results are compared with the M_{pk} = 0.1 case, near the liner trailing-edge some deviation is observed from the experimental data for the time-domain result. However, the agreement between the simulations is good. The wall-impedance jumps are influential at this frequency.

4.2.3 $M_{pk} = 0.5$ Case

Numerical instabilities were more violent at this Mach number. For this reason, we could not obtain a solution at $f = 0.5$ kHz and 1.0 kHz on a 344x14 mesh. But we overcame these numerical instabilities by reducing the mesh resolution for the 1.0 kHz frequency. For this case, a 188x14 mesh was used and a 344x14 mesh was used for the other frequencies with a mesh resolution of 23 cells per wavelength for the highest frequency (3.0 kHz).

Figure 4.19 displays and compares the results for the case of $f = 1.0$ kHz. The solid line represents the frequency-domain result, the dashed-dotted-dotted line represents the time-domain result, and symbol indicates the experimental data at all figures in this subsection. Since we encountered numerical instabilities, the simulation was performed with a grid resolution of 37 cells per wavelength (188x 14 mesh) for this frequency. This resolution is still very sufficient to obtain a solution. It should be recalled from section 3.4 that the maximum grid resolution allowable for numerical stability was $\lambda_x/\Delta x = 44$.

Comparison with the $M_{pk} = 0.1$ and $M_{pk} = 0.3$ cases indicates an improvement in the results. The agreement between the computations and experiment is very good. It should be noted that no experimental data was shown after a constant microphone location for the same reason as explained in the previous section for the 1.0 kHz case at $M_{pk} = 0.3$.

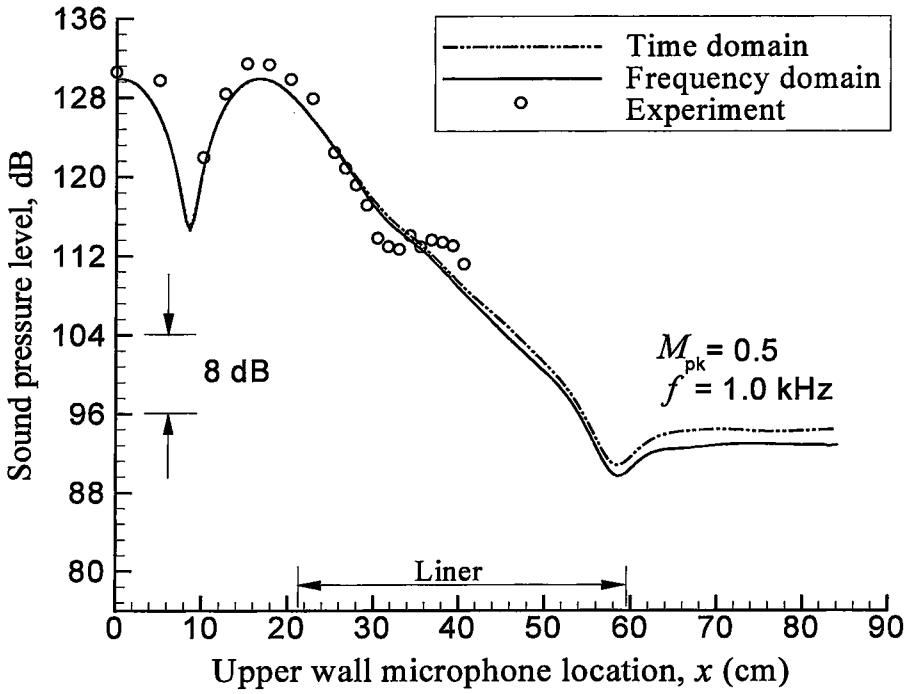

Figure 4.19 Sound pressure level along the upper wall given by frequency and time-domain simulations, and experiment at f = 1.0 kHz and M_{pk} = 0.5.

Comparisons between numerical results and experimental data for the case of f = 1.5 kHz are shown in Fig. 4.20. The frequency-domain and time-domain results seem to be identical. When the results are compared with the M_{pk} = 0.1 and M_{pk} = 0.3 cases, near the liner trailing-edge the both numerical results (frequency and time-domain) appear to deviate from the experimental data.

In Figure 4.21 the results are compared for the case of f = 2.0 kHz. An improvement is observed when the frequency-domain simulation is compared with the M_{pk}= 0.1 and the M_{pk}= 0.3 cases. The frequency-domain result agrees well with the time-domain result and experimental data.

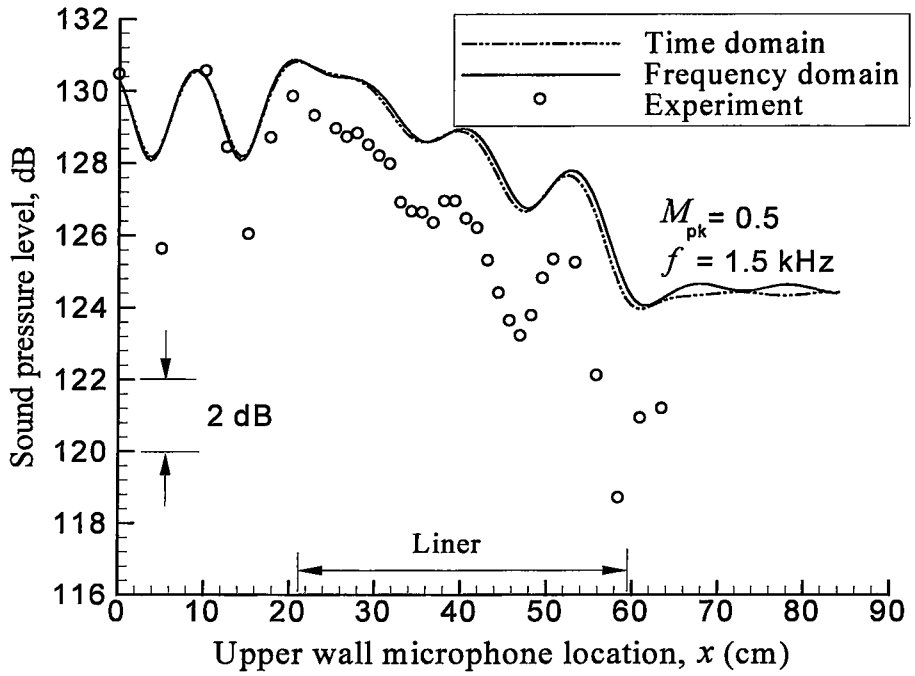

Figure 4.20 Sound pressure level along the upper wall given by frequency and time-domain simulations, and experiment at f = 1.5 kHz and M_{pk} = 0.5.

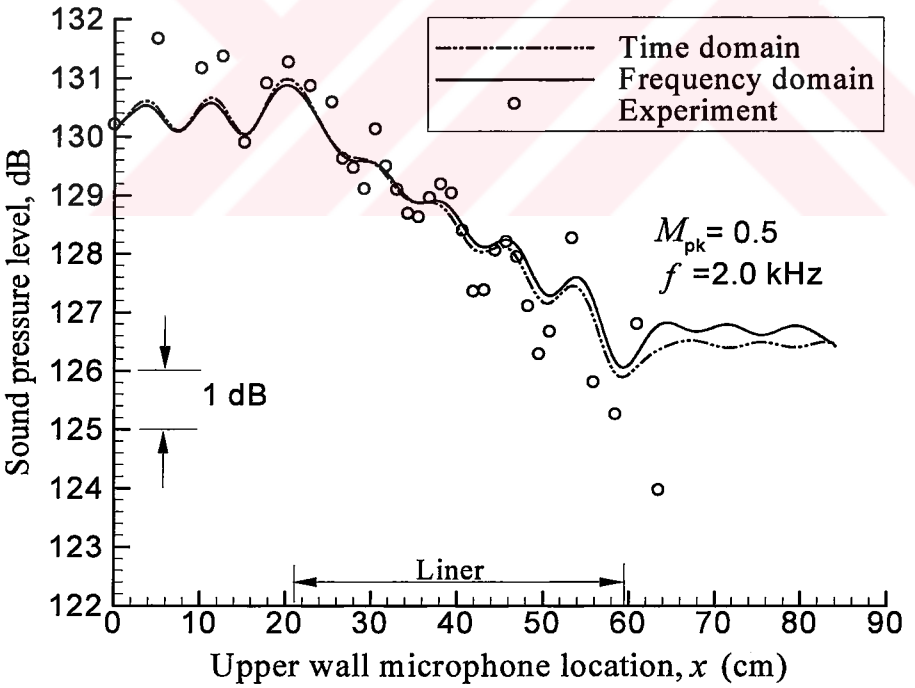

Figure 4.21 Sound pressure level along the upper wall given by frequency and time-domain simulations, and experiment at f = 2.0 kHz and M_{pk} = 0.5.

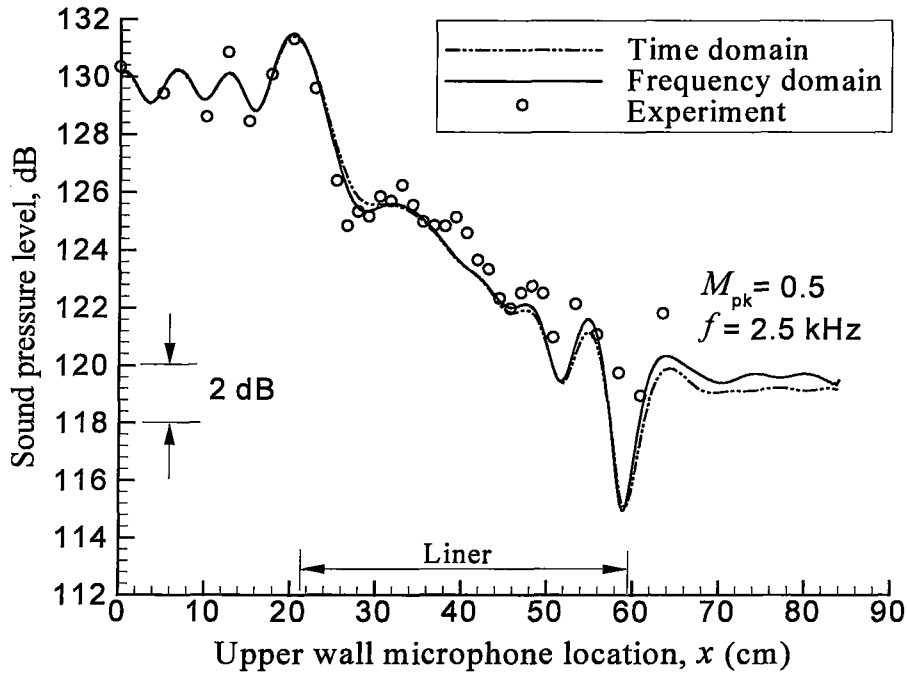

Figure 4.22 Sound pressure level along the upper wall given by frequency and time-domain simulations, and experiment at f = 2.5 kHz and M_{pk} = 0.5.

In Figure 4.22 the results are compared for the case of f = 2.5 kHz. The trends for the calculated SPLs in the frequency-domain simulation follow well those for the time-domain simulation and experiment. Large SPL variations are observed in the liner leading- and trailing-edge regions, because of increased wave reinforcements and cancellations.

Figure 4.23 shows and compares the results for the case of f = 3.0 kHz. The frequency-domain result agrees with the experimental data somewhat better than the time-domain result. When the results are compared with M_{pk} = 0.1, in the liner trailing-edge region the time-domain result appears to deviate from the experimental data and from the frequency-domain result. However, the agreement between the numerical results is good in general.

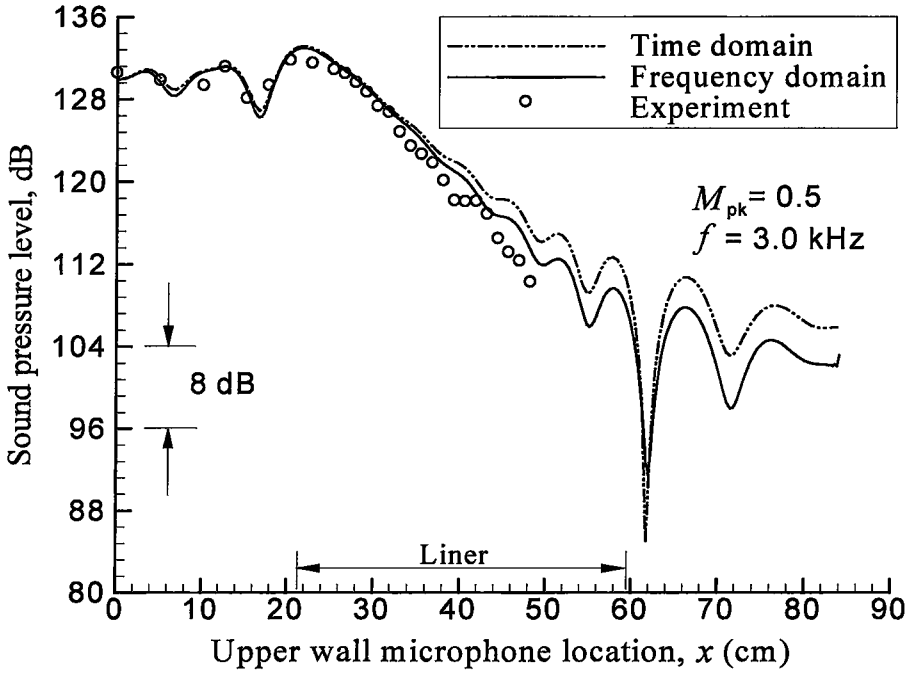

Figure 4.23 Sound pressure level along the upper wall given by frequency and time-domain simulations, and experiment at f = 3.0 kHz and M_{pk} = 0.5.

4.3 Requirement for Computational Resources

In this study, simulations were performed using Fortran 90. A simulation on a 188x14 mesh using 30000 iteration levels required 3158 second CPU time on a Pentium II processor (233 MHz). Memory requirement for this code is about 1.8Mb. For a single grid point, about 40 microseconds was spent per grid points per iteration

CHAPTER 5

CONCLUSION

Numerical simulations of sound propagation in a flow-impedance tube in frequency domain have been performed comparing results with those of the time-domain simulations that were performed previously [16]. The simulations were performed using the NASA Langley flow-impedance tube for frequencies of 0.5 to 3.0 kHz with 0.5 kHz increments at Mach numbers 0.1, 0.3, and 0.5 with sheared background flows.

In the simulations, the same mathematical model as that of the time-domain method was used. In other words, the linearized 2D Euler equations were used as the governing equations, unlike the common frequency domain approaches [21]. The classical acoustic impedance condition [12] given for frequency-domain analyses was applied on the acoustic treatment panel. All time-domain conditions and equations were transformed to frequency domain. Our first attempt for the solution of these equations was to use a direct method; LU-decomposition with full pivoting. Sufficient grid resolution could not be attained for solutions because of the excessive memory requirement. Therefore, as a second attempt, pseudo time-marching of the equations was considered to reduce the computational cost and memory requirement. In this method, a pseudo time derivative was added to each equation

and the four-stage compact Runge-Kutta scheme was applied to solve the equations iteratively. Stability analysis indicated that this algorithm is conditionally stable. To increase the stability of the solution, boundary conditions were applied implicitly using the solution from the interior domain at every iteration level.

Since the same flow and acoustic source conditions as well as the mathematical model as the time-domain method were used, it was expected that the results from both methods would agree well. Although there were small differences, the results indicated good agreement with the time-domain results and experimental data. However, the scheme became unstable for 0.5 kHz at M_{pk} = 0.3 case and 0.5 and 1.0 kHz at M_{pk} = 0.5 case because of the excessive grid resolution and insufficient background dissipation which were designed to handle 3.0 kHz components. To overcome these numerical instabilities, grid resolution was decreased, but still for the frequency of 0.5 kHz at M_{pk} = 0.5 case the simulation failed because the grid was still too fine. Lowering the grid resolution further could have given a solution, but this was not done.

The comparisons of the frequency domain results with experimental data and the results of the time domain studies of reference [16] indicated good agreement in general. Although the method as presented here is restricted to two-dimensional rectangular ducts, it may be extended to curvilinear boundaries and to three dimensions.

REFERENCES

[1] Pierce, A.D., "Acoustics An Introduction to Its Physical Principles and Applications," Acoustical Society of America,1991.

[2] Kerrebrock, J,K., "Aircraft Engines and Gas Turbines," MIT press, 1984.

[3] White, F.A., " Our Acoustic Environment," John Wiley & Sons, 1975.

[4] Notes from Course by Özyörük, Y., "AEE 548 Fundamentals of Aerodynamic Noise," METU, Spring 1999

[5] Summary from Journal of the Acoustical Society of America "Sound Absorbtion," Web page.

[6] Meyer, E., and Neumann, E.G., "Physical and Applied Acoustics," Academic Press, New York and London, 1972.

[7] Kinsler, E.L., and Frey, A.R., " Fundamentals of Acoustics," John Wiley & Sons, 1975.

[8] Nahfeh, A.H., Kaiser, J.E., and Telionis, D.P., "Acoustics of Aircraft Engine-Duct Systems," AIAA Journal, 13(2), pp.130-153, September 1973.

[9] Tam, C.K.W., and Auriault, L., "Time-Domain Impedance Conditions for Computational Aeroacoustics," AIAA Journal, 34(5), pp.917-923, May 1996.

[10] Morse, P.M., and Ingard, K.U., "Theoretical Acoustics," Mcgraw-Hill, 1968.

[11] Özyörük, Y., Long, L.N., and Jones, M.G., "Time-Domain Numerical Simulation of a Flow Impedance Tube," Journal of Computational Physics, 146(1), pp.29-57, October 1998.

[12] Myers, M.K., "On the Acoustic Boundary Condition in the Presence of Flow," Journal of sound and Vibration, 71(3), pp.429-434,1980.

[13] Unruh, J.F., and Eversman,W., "The Transmission of Sound in an Acoustically Treated Rectangular Duct with Boundary Layer," J. of Sound and Vibration, 25(3), pp.371-382, 1972

[14] Watson, W.R., Jones, M.G., Parrot, T.L., and Tanner, S.E., "Validation of a Propagation Model Method for Determining Liner Impedance," ASME, 1995

[15] Watson, W.R., Jones, M.G., Parrot, T.L., and Tanner, S.E., "A Finite element Propagation Model for Extracting Normal Incidence Impedance in Nonprogressive Acoustic Wave Fields," j.Comput. Phys. 125,177(1996).

[16] Özyörük, Y., and Long, L.N., "Time-Domain Calculation of Sound Propagation in Lined Ducts With Sheared Flows," AIAA Journal, 38(5), pp.768-773, May 2000.

[17] Özyörük, Y., and Long, L.N., "A Time-Domain Implementation of Surface Acoustic Impedance Condition with and Without Flow," J. of Computational Acoustics, 5(3), pp. 277-296, 1997.

[18] Giles, M.B., "Nonreflecting Boundary Conditions for Euler Equation Calculations," AIAA Journal, 28(12), pp.2050-2058, December 1990.

[19] Özyörük, Y., and Long, L.N., "Time-Domain Calculation of Sound Propagation in Lined Ducts with Sheared Flow," AIAA Paper 99-1817, May 1999.

[20] Thompson, K.W., "Time-Dependent Boundary Conditions for Hyperbolic Systems, II," Journal of Compuational Physics, vol.89, pp.439-461, 1990.

[21] Watson, W.R., Jones, M.G., and Parrot, T.L., "Experimental Validation of a Two- Dimensional Shear-Flow Model for Determining Acoustic Impedance," Technical report TP-2679(NASA, Washington.DC.1987).

[22] Özyörük, Y., and Long, L.N., "Impedance Boundary Conditions for Time-Domain Computatioal Aeroacoustics Methods," AIAA Paper 97-0021, 35th Aaerospace Science Meeting & Exhibit.

[23] Hoffmann,K.A., and Chiang,S.T., "Computational Fluid Dynamics for Engineers," Engineering Education System, USA, 1995

[24] Hirsch, C., "Numerical computation of Internal and External Flows," John Wiley & Sons

APPENDIX A

FINITE DIFFERENCE FORMULAS USED IN THIS STUDY

As shown in Fig. 3.1 the walls are placed midway between two grid points. Therefore, ghost grid points are defined at location $j = 1$ and $j = N_y$, but the wall conditions are applied at $j = 3/2$ and $j = N_y$–(1/2), where wall derivative, $(\partial Q/\partial y)_{i,\,3/2}$ and $(\partial Q/\partial y)_{i,\,N_y\text{-}(1/2)}$, are required. In the space-discretized formulas N_x and N_y denote the maximum number of grid point in the x- and y-direction, respectively.

A.1 First-order Derivatives in the x-direction

At inlet where $i = 1$. The forward difference formula is

$$\left(\frac{\partial Q}{\partial x}\right)_{i,j} = \frac{-22Q_{i,j} + 36Q_{i+1,j} - 18Q_{i+2,j} + 4Q_{i+3,j}}{12\,\Delta x} + O(\Delta x^3) \qquad (1)$$

At outlet where $i = N_x$. The backward difference formula is

$$\left(\frac{\partial Q}{\partial x}\right)_{i,j} = \frac{22Q_{i,j} - 36Q_{i-1,j} + 18Q_{i-2,j} - 4Q_{i-3,j}}{12\,\Delta x} + O(\Delta x^3) \qquad (2)$$

Near the inlet where $i = 2$. The difference formula is

$$\left(\frac{\partial Q}{\partial x}\right)_{i,j} = \frac{-3Q_{i-1,j} - 10Q_{i,j} - 18Q_{i+1,j} - 6Q_{i+2,j} + Q_{i+3,j}}{12\,\Delta x} + O(\Delta x^4) \qquad (3)$$

Near the outlet where $i = N_x$-1. The difference formula is

$$\left(\frac{\partial Q}{\partial x}\right)_{i,j} = \frac{3Q_{i+1,j} + 10Q_{i,j} + 18Q_{i-1,j} + 6Q_{i-2,j} - Q_{i-3,j}}{12\,\Delta x.} + O(\Delta x^4) \qquad (4)$$

In the interior where $i = 3,..., N_x$-2. The central difference formula is

$$\left(\frac{\partial Q}{\partial x}\right)_{i,j} = \frac{Q_{i-2,j} - 8Q_{i-1,j} + 8Q_{i+1,j} - Q_{i+2,j}}{12\,\Delta x} + O(\Delta x^4) \qquad (5)$$

where $j = 3/2,..., N_y$-1/2 and Q is any variable.

A.2 First-order Derivatives in the y-direction

At the lower wall where $j = 3/2$. $Q_{i,1}$ is ghost point quantity. The wall derivative is

$$\left(\frac{\partial Q}{\partial y}\right)_{i,\frac{3}{2}} = \frac{-46Q_{i,1} + 42Q_{i,2} + 6Q_{i,3} - 2Q_{i,4}}{48\,\Delta y} + O(\Delta y^3) \qquad (6)$$

At the upper wall where $j = N_y$-(1/2). Q_{i,N_y} is ghost point quantity. The wall derivative is

$$\left(\frac{\partial Q}{\partial y}\right)_{i,N_y-\frac{1}{2}} = \frac{46Q_{i,N_y} - 42Q_{i,N_y-1} - 6Q_{i,N_y-2} + 2Q_{i,N_y-3}}{48\,\Delta y} + O(\Delta y^3) \qquad (7)$$

Near the lower wall where $j = 2$. $Q_{i,j-1}$ is ghost point quantity. The difference formula is

$$\left(\frac{\partial Q}{\partial y}\right)_{i,j} = \frac{-3Q_{i,j-1} - 10Q_{i,j} - 18Q_{i,j+1} - 6Q_{i,j+2} + Q_{i,j+3}}{12\,\Delta y} + O(\Delta y^4) \qquad (8)$$

Near the upper wall where $j = N_y$-1. $Q_{i,j-1}$ is ghost point quantity. The difference formula is

$$\left(\frac{\partial Q}{\partial y}\right)_{i,j} = \frac{3Q_{i,j+1} + 10Q_{i,j} + 18Q_{i,j-1} + 6Q_{i,j-2} - Q_{i,j-3}}{12\,\Delta y} + O(\Delta y^4) \qquad (9)$$

In the interior where $j = 3,..., j$-2. When j =3 and $j = N_y$-2, $Q_{i,j-2}$ and $Q_{i,j+2}$ are ghost point quantities, respectively. The central difference formula is

$$\left(\frac{\partial Q}{\partial y}\right)_{i,j} = \frac{Q_{i,j-2} - 8Q_{i,j-1} + 8Q_{i,j+1} - Q_{i,j+2}}{12\,\Delta y} + O(\Delta y^4) \qquad (10)$$

where $i = 1,..., N_x$.